

Finding persistent sources with the BeppoSAX/WFC: a in-depth analysis

F. Capitanio¹, A. J. Bird², M. Fiocchi¹, S. Scaringi³, P. Ubertini¹

ABSTRACT

During the operational life of the Italian/Dutch X-ray satellite (1996-2002), BeppoSAX, its two Wide Field Cameras performed observations that covered the full sky at different epochs. Although the majority of analysis performed on BeppoSAX WFC data concentrated on the detection of transient sources, we have now applied the same techniques developed for the *INTEGRAL*/IBIS survey to produce the same work with the BeppoSAX WFC data. This work represents the first unbiased source list compilation produced from the overall WFC data set optimised for faint persistent sources detection. This approach recovers 182 more sources compared to the previous WFC catalogue reported in Verrecchia et al. (2007). The catalogue contains 404 sources detected between 3-17 keV, 10 of which are yet to be seen by the new generation of telescopes.

Subject headings:

1. Introduction

The two Wide Field Cameras (WFCs) (Jager et al. 1997) on board the BeppoSAX satellite (Boella et al. 1997), were mounted 180 degrees away from each other and pointed perpendicular to the direction of the Narrow Field Instruments (NFI), hence looking at two different sky zones during each NFI pointing. In this way, over the 6 years operational life of BeppoSAX, the WFCs observations covered almost all the sky with at least one pointing (typically 100 ks duration). This serendipitous observing strategy, during which the WFCs acted as secondary instruments, was driven by the approved Narrow Field Instrument observing programme. However, twice a year, for around 8% of the total observing time of

¹INAF IASF-Roma, Via Fosso del Cavaliere 100, 00033 Rome, Italy

²School of Physics and Astronomy, University of Southampton, Highfield, Southampton, SO17 1BJ, UK

³Department of Astrophysics, Radboud University Nijmegen, PO Box 9010, 6500 GL Nijmegen, The Netherlands

the satellite, the WFCs observed the Galactic bulge region as primary instruments (i.e. thanks to a pre-planned observing programme) collecting a total exposure on the Galactic Centre of 6 Ms during the operational life of the satellite.

The WFCs were coded mask instruments characterised by a large ($40\text{ deg} \times 40\text{ deg}$) field of view, a good angular resolution (few arcmin) and a pointing strategy that permitted all the sky to be observed during the satellite’s operational life. The operating principles are reported in detail in Jager et al. (1997). The principal scientific objective of the WFCs on BeppoSAX was the study of the X-ray variability of the sky. In fact, through the serendipitous monitoring of large sky regions, the WFCs were able to detect a lot of transients X-ray events like GRBs and X-ray binary outbursts (see e.g. Piro & Scarsi 2004, and reference therein). Most of the time, the WFCs were used as triggers for follow-up studies with higher-sensitivity narrow-field instruments on BeppoSAX itself or on other platforms. The principal characteristics of the WFCs are briefly summarised in Table 1.

The goal of our study is to reanalyse the WFC data so as to obtain a static view of the sky averaged all over the six years of BeppoSAX operational life in order to search for faint persistent sources that remained hidden in the previous analyses because they were too faint to be detected with an adequate confidence level in a single observation.

This work is thus complementary to the previous WFC survey analysis reported (Verrecchia et al. 2007) and it is a natural evolution of the work developed for the IBIS/INTEGRAL survey catalogue (Bird et al. 2010). Indeed, the WFC principal characteristics are directly comparable with those of IBIS (Ubertini et al. 2003), the coded mask gamma-ray telescope on board the *INTEGRAL* satellite (Winkler et al. 2003). The aim of this paper is therefore to apply the same techniques developed for the IBIS survey (Bird et al. 2004, 2006, 2007, 2010) to the BeppoSAX WFC data, searching for faint persistent sources in the total mosaic maps made from individual WFC sky images. IBIS and the SAX WFCs have a complementary and partially overlapping energy range (3-28 keV for WFCs and 17 keV - 1 MeV for IBIS), allowing studies of persistent sources over a larger energy range. Results from this work have also been used to give an independent check of some of the fainter sources detected in the IBIS survey catalogue production: details of the correlation between IBIS and WFC detections can be found in Capitanio et al. (2010)

2. WFC Sky Map Production

The WFC data are organised in short observational periods (OPs) of at least 100 ks. We collected all the available data from different archives and analysed all the collected OPs

with the WFC Data Analysis System, extracting images in the 3-17 keV and 18-28 keV energy ranges. The data analysis up to and including the image level has been performed with the final version of the WFC standard data analysis software¹ (Jager et al. 1992) using the reference catalogue included in the software package.

The WFC standard software uses the IROS method (Iterative Removal of Sources) to extract sources from the shadowgrams of the WFCs coded masks (in ’t Zand et al. 1992). During this procedure we used specific parameters included in the standard software in order to keep all the detected sources in the second and subsequent IROS iterations indepenently of the source identification (‘-m4’ option within the standard software). Moreover we lowered the IROS threshold (allowing up to 300 iterations), such that the source removal continued further into the low significance detections and/or noise than would normally be done for transient detection, retaining low significance information for the mosaicing process.

We subsequently applied a filter in order to eliminate corrupted and noisy images by comparing the root main square (rms) and mean of each flux image against the average image rms and image mean level derived from all images. Any images with an rms or mean level more than 5 sigma away from the nominal average values were not incorporated into the final mosaic. After the filtering procedure, about 95% of the total initial number of OPs were used in the subsequent analysis.

An all-sky mosaic of the images has been generated using the same software used for the IBIS survey (Bird et al. 2004, 2006, 2007, 2010). The mosaicing procedure is designed to average a large number of small single images that cover almost all the sky into a single

¹www.asdc.asi.it/bepposax/software/index.html

Table 1: *BeppoSAX* WFCs principal characteristics.

parameter	WFC value
Energy range	3-28 keV
Energy resolution	20% at 6 keV
Effective area	140 cm^2
Field of view	40° × 40° (FWZR) 20° × 20° (FWHM)
Angular Resolving Power	5’
Source location accuracy	< 1’
Sensitivity in 10 ⁵ s	~1 mCrab (3-28 keV)

all-sky image. Thus the images of the filtered OPs have been combined together into all-sky mosaics. For each sky pixel, the mosaic software establishes a weighted mean flux, weighting each input image contribution according to the variance of the signal in each input pixel. The events are fully redistributed in the final sky map pixels that oversample the original image pixels and system PSF. The process generates flux, error, significance and exposure mosaic images.

This procedure is strongly tuned towards the detection of persistent (and weak) sources. Even if a source field has been observed for a long time, intrinsic variability of a source may mean that it is detected only in few individual images, and it will not be detectable in the final map.

The signal to noise ratio of a persistent source will increase with the number of added images. Conversely, noise and imaging artefacts in individual OP images that would create false detections are, by their very nature, detected in the same positions in only one image, and will be lost into the mosaic background provided that two conditions are satisfied:

- many images must be summed together (we assume a conservative minimum value for the exposure of 1.4 Ms - at least 14 images considering that the maximum possible exposure of a single image is 100 ks). In the regions of the map with an exposure less than this value, we did not consider any detection that was not reported before in the catalogue of Verrecchia et al. (2007).
- the averaging procedure could fail to eliminate the false detections if they are due to systematic image artefacts resulting from the image reconstruction process if the sky pointing direction of the telescope is repeated. In this way, systematic effects will appear in the same sky positions and will be summed during the mosaic process. However, this is not the case of the WFC images due to their random pointings deriving from the serendipitous nature of the observing programme (this kind of effect cannot be totally excluded for the galactic centre region, details in Sections 2.1 and 4.2.1)

Moreover the mosaic procedure, as it combines many images from many pointings, averages any differences due to the off-axis response that are not completely corrected by the software (see Verrecchia et al. (2007) for details). Also the Earth occultation simply contributes to the background of the final mosaic.

The collected data covered all the sky - although not uniformly. In fact, as Figure 1 shows, there are zones with much higher exposure such as the Galactic center and the fields centered on the North and South Celestial poles due to the observing strategy and manouvering techniques of the *BeppoSAX* satellite (Tramutola et al. 2000). The average

exposure over the entire map is about 4×10^6 s, even if there are some regions with an exposure of two orders of magnitude less and others where the exposure reaches $\sim 2 \times 10^7$ s. There are two principal regions of low exposure: the zone around Sco X-1 (Sco X-1 was so bright that all the data containing this source in the field of view were corrupted) and two small zones of about 5 degree radius 180 degrees apart at coordinates (l,b)=(120.2°, -57.4°) and (299.0°, 68.2°).

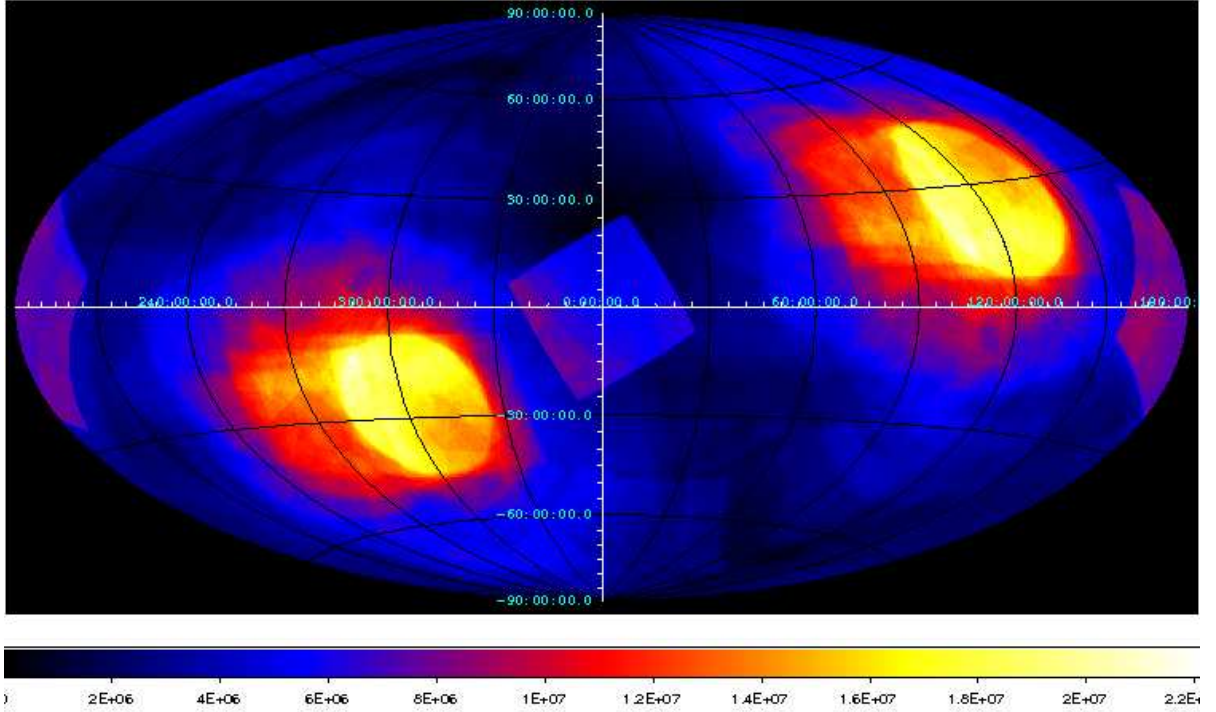


Fig. 1.— The WFC mosaic exposure map (in seconds) in Galactic Coordinates. The two zones with higher exposure are due to the polar passages of the Extended Science mode one (ESM1) and two (ESM2) (Tramutola et al. 2000); the high exposures on the Galactic Centre and the Anti-center zones are due to the WFC core program observations of the Galactic Centre region.

The higher energy range map (18-28 keV) is affected by more noise and larger distortion of the Point Spread Function (see Section 2.1). Thus for source searching we only use the 3-17 keV map.

It is clear that the analysis of WFC data carried out so far has concentrated on locating transient sources, whereas our methods allow a much more efficient detection of weak persistent sources: as an example Figure 2 shows a zoom of the all-sky WFC map (3-17 keV) around GX301-2: the sources indicated with white labels have been reported in both our and Verrecchia et al. (2007) catalogues, while the sources labelled in yellow have been

reported only in our catalogue. The three sources with yellow labels are classified as faint persistent (even if variable) sources (see e.g. Bird et al. (2010)). The flux of the sources present in Figure 2 in both catalogues are reported in Table 2

Table 2: Fluxes of sources shown in the sky field of Figure 2. flux_{ver} is the average flux extrapolated from Verrecchia et al. (2007) (the large errors represent the source variability rather than an intrinsic measurement uncertainty), $\text{flux}_{\text{mosa}}$ is the flux derived from the all-sky mosaic map taken from Table 3.

source name	$\text{flux}_{\text{mosa}}$ (3-17 keV)mCrab	flux_{ver} (2-10 keV) mCrab
-		
GX301-2	20.3 ± 2.1	18 ± 26
4U 1323-619	4.9 ± 0.5	7 ± 5
IGR J12349-6434	0.6 ± 0.1	-
IGR J13020-6359	0.4 ± 0.1	-
H 1249-637	0.7 ± 0.1	-

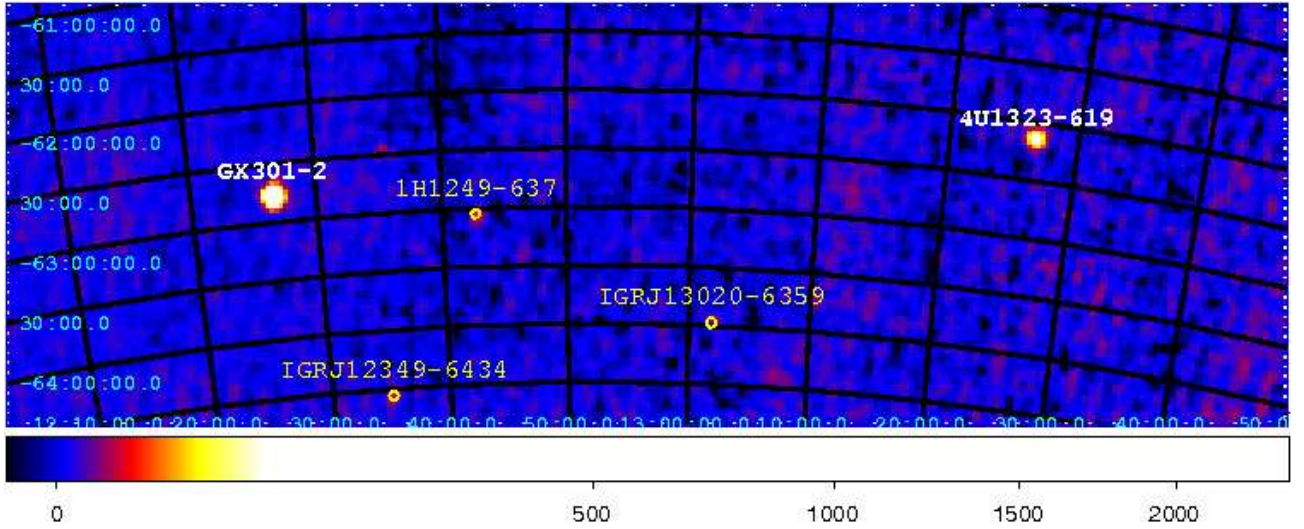


Fig. 2.— Zoom of the WFC final mosaic map (in units of sigma) centred around the GX301-2 field. The sources indicated in yellow have been reported only by our catalogue, while those with white labels have been reported in both our and Verrecchia et al. (2007) catalogues

Finally, Figure 3 shows the 3-17 keV WFC final sky map in units of σ . The symbols represent the detected source positions, the parts of the map in red are zones with high level of noise (i.e. the Galactic and Anti-Galactic Centre).

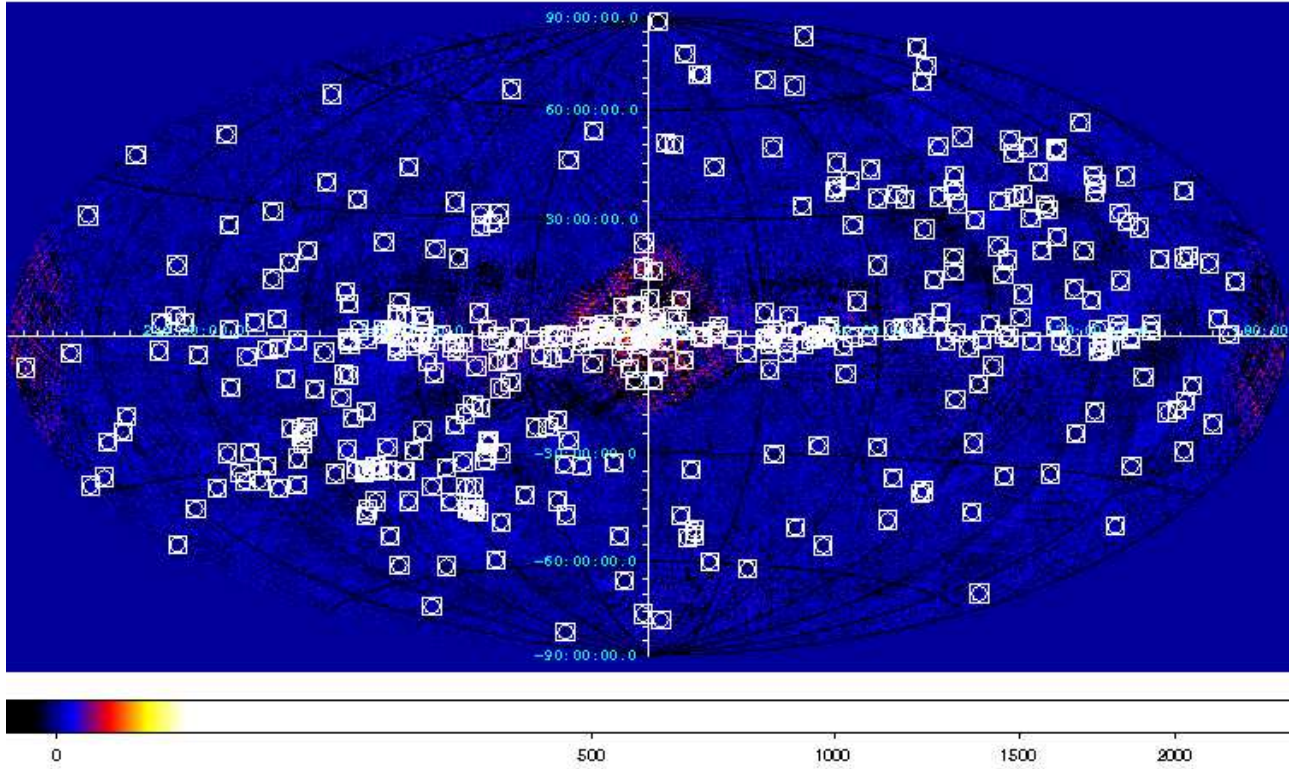


Fig. 3.— WFCs final mosaic between 3-17 keV in units of sigma. The symbols represent the detected sources positions. The parts of the map around the Crab and the Galactic Centre, present a higher level of noise.

2.1. Image problems - the ‘comet’ effect and noisy regions

The IROS procedure performs a cross-correlation between the detector image and the mask pattern via a matrix multiplication during every iteration and the detections are localised by fitting any peaks with an expected Point Spread Function (PSF). After the positions are compared with a reference catalogue, the effect of sources on the detector plane are then simulated and subtracted. Because each source is not simulated in exactly the same position in each single OP image (in ’t Zand et al. 1992), this results in a slight broadening of the final PSF in the mosaic image.

The PSF can also be different from one single observation to the next as a result of photon penetration into the WFC detector gas chamber. This effect becomes more evident both at higher energy ranges and at large off-axis angle detections, and hence can change between OPs as the pointing direction changes.

In fact as reported in in 't Zand et al. (1992), the photons can be absorbed at any depth d within the WFC detector. The probability of absorption of a photon in a Δd thick layer at a depth d is proportional to:

$$P(d) \propto e^{-d/l(E)} T(d) \Delta d;$$

where $l(E)$ is the mean free path of a photon with an energy E and $T(d)$ represents the blocking by the three WFC detector wire grids and the cut-off due to the finite detector thickness.

The projection of $P(d)$ on to the sky plane influences the PSF. This takes the form of $D(E)\tan\alpha$ where $D(E)$ is the maximum depth for photons of energy E and α is the off-axis angle.

Thus the photon distribution projected on the detector plane at energies above ~ 15 keV shows an asymmetric tail which cuts off at positions corresponding to that of the grid planes and to the bottom of the detector (i.e. 3 mm on the detector plane for a source at an off-axis angle of 4° at 30 keV. See in 't Zand et al. (1992) for further details).

These effects have a significant impact on the source PSFs in the total map, creating a sort of ‘comet effect’ in the PSF shape that becomes worse at higher energies, as Figure 4 shows. Thus for source searching we choose the 3-17 keV energy range in order to both maximise the instrument sensitivity and minimize the deformation of the PSF in the maps.

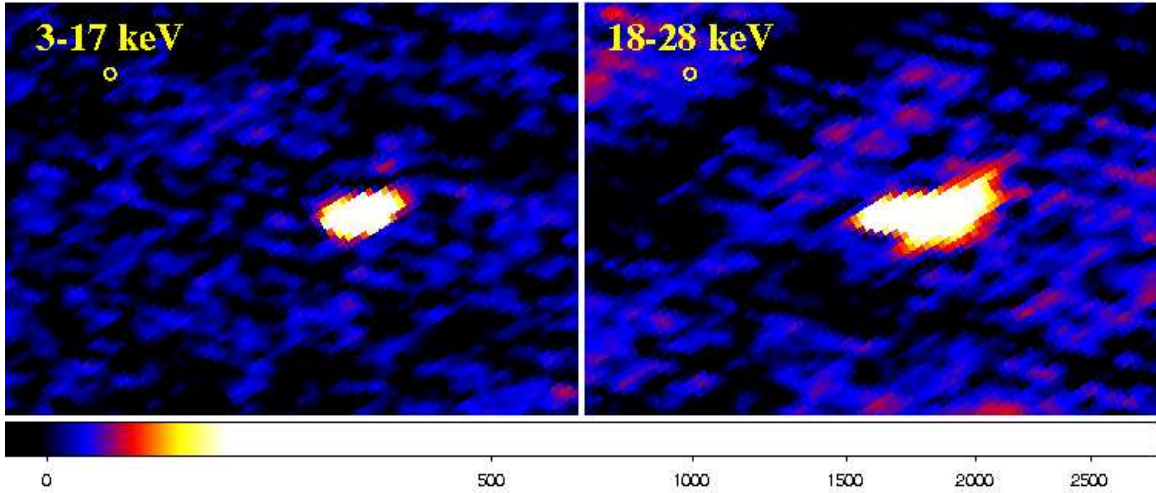


Fig. 4.— Zoom of the final mosaic map (expressed in sigma) on the Crab nebula in the two energy ranges (left: 3-17 keV, right: 18-28 keV) showing that the distortion of the PSF (‘Comet effect’) is more evident at high energies.

Following the failure of the gyroscopes on board the satellite, the star trackers were used to control the rotations and the pointing of the satellite (Tramutola et al. 2000). This procedure required those zones of the sky regularly observed (such as the Galactic Centre

region and consequently the anti-galactic centre and the zone around the Crab nebula) to be observed with the satellite (and WFC detector) in the same position with respect to the sky, thus with the same bright stars in the star tracker field of view. As the *INTEGRAL* pointing strategy has demonstrated for coded mask instruments, observing the same sky zone with different pointing configurations can significantly reduce the background (Courvoisier et al. 2003) image artefacts. For this reason, the Galactic Centre zone (and the anti-Centre) have a significantly higher background in the WFC total mosaic map compared to the other sky zones where the serendipitous nature of the pointings have the same effect as the *INTEGRAL* pointing strategy. Moreover the Galactic centre zone has an intrinsically higher noise also in a single image, due to the presence of a large number of sources in the field of view which make the image deconvolution more difficult.

3. The Table

3.1. Source List Generation

Two methods were used to create an initial source list. The first used a tool developed for the IBIS survey (Bird et al. 2007) that searched for excesses exceeding a local threshold set by a baseline statistical threshold scaled by the local rms fluctuations within the map. This tool is intended to suppress the detection of fake sources in areas of the map with high non-statistical fluctuations. A second method based on SExtractor 2.4.4 software (Bertin & Arnouts 1996) has been used to cross check the results with a bandpass filter (Gauss filter) to minimize the source confusion in crowded fields. The list of excesses was then checked manually. A baseline acceptance limit at 4.8 sigma level has been adopted, although we stress again that the effective threshold in areas of high systematic artefacts will be considerably higher thus the acceptance limit varies considerably from zone to zone of the map. For example in the Galactic Centre region the local acceptance limit is at $\sim 12\sigma$. After acceptance, the source positions and fluxes were evaluated using a barycentering method to determine the centroid of the source profile. The mean flux of the sources was determined from the count rate at the position of the source maximum significance (the counts-to-flux conversion is obtained assuming a Crab-like spectrum for the sources). After all the checks, the final list contains 458 excesses above 4.8 sigma. Of these excesses, 404 were identified as sources while 54 were considered to be map artefacts because of the PSF shape or the proximity to an image structure. The sources in the final list were then classified by a process of correlation with other existing catalogues.

3.2. Position error

The PSF distortion due to the ‘comet effect’ and the presence of other systematic effects prevent us from simply extrapolating the point location accuracy from the mosaic maps with a fixed confidence level. In order to estimate the source location error radius of the WFC sources, we compared the positions of the known sources detected in the map with their best known positions, applying a procedure similar to the one reported in Scaringi et al. (2010b). The best positions were extracted from the *INTEGRAL general reference catalogue (IGRC)*, considered to be one of the most recent and comprehensive compilations of accurate X-ray and hard X-ray positions (Ebisawa et al. 2003). We have taken into account only those sources in the IGRC with a position specified to better than $30''$, i.e. those providing a well-defined ‘reference’ position; this was possible for a total of 204 sources detected by the WFC. Following the procedure described in Scaringi et al. (2010b), we plotted the offset between our positions and the reference ones, as a function of the WFCs Signal to Noise Ratio (SNR) for these 204 sources, after which we binned the offset values in order to have enough statistical significance for each bin. This method can take into account both the systematic and the statistical errors as it makes no assumptions about the form of the position error. The best fit curve for the 90% confidence radius, plotted in Figure 5, is: $Y = \frac{A(0)}{X}e^{A(1)} + A(2)$; where: $A(0)=3.21$; $A(1)=1.41$; $A(2)= 1.56$; The errors reported in Table 3 are extrapolated from Figure 5.

It is important to note that the best positions for variable and transient sources are generally derived from the single observation with the highest sigma. The positions derived from the overall mosaic for these sources are essentially degraded by the many non-detections added when forming the final mosaic. Conversely, for faint persistent sources, the position extracted from the mosaics is the best that can be obtained, and has the lowest error.

3.3. Comparison with the previous WFC catalogue

A WFC catalogue of sources was published by Verrecchia et al. in July 2007. That work is based on the analysis of each single pointing and is optimised for transient source detection (a similar work, restricted to the Galactic plane zone, was published in Capitanio et al. (2004)). Our work is instead based on the searching of mosaic maps and is primarily intended to identify persistent sources not necessarily visible in a single OP. For this reason our list of sources is somewhat different from the one published in Verrecchia et al. (2007).

Verrecchia et al. (2007) lists 253 sources while our catalogue contains 404 sources; 222 sources are present in both catalogues. The 31 sources reported only in Verrecchia et al.

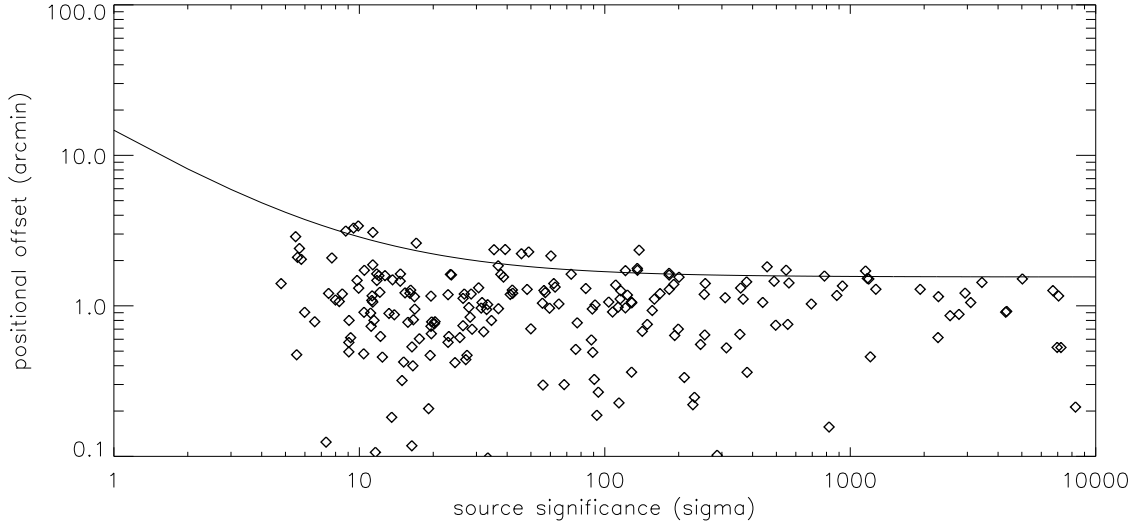


Fig. 5.— Offsets between the WFC map positions and IGRC positions as a function of source SNR. The curve represents the extrapolated error (90% confidence limit).

(2007) are all faint sources detected in only one or two individual OPs, thus as we expected they are not detected in the total map. In particular, within the 11 brightest sources listed only by Verrecchia et al. (2007), there are 5 sources for which there is a detection in the total map but the detection level is lower than 4.8 sigma. The other 6 sources are located near structures in our map or in noisy regions (like the Galactic centre region) where the detection threshold is high.

As we expected, the 182 sources found only by us (shown in bold in Table 3) are mostly persistent or quasi persistent. It is important to note that within these 182 sources, there are 17 IGR sources and 9 *Swift* sources that have been discovered only after the end of the Beppo SAX mission. Moreover, the list contains ten new sources.

In order to verify and further quantify the intrinsic variability of the source populations in the two catalogues, we have inspected the statistical properties of light curves extract for each source. We developed a tool for WFC light curve production, that reads the flux (counts/s/cm²) from the source position in each single WFC pointing image using the *The IDL Astronomy User's Library procedures*². Unfortunately, any tool such as this will be affected by the problem reported by Verrecchia et al. (2007): the WFCs standard software does not totally correct the differences in flux due to the different position of the sources in

²<http://idlastro.gsfc.nasa.gov/>

the field of view of each WFC pointing. This effect adds a systematic error of about 10%.

The intrinsic variability for each source in our dataset was determined by performing a check for excess variance (i.e a chi-squared test against a constant mean flux) for each of the light curves. As expected, the χ^2 distribution is peaked around 1 (indicating a persistent source) with a long tail representing the variable sources (see Figure 6). Moreover, as Figure 7 shows, comparing the variability statistic of both the sources detected also in the previous catalogue and the sources detected only in this catalogue, it is clear that the former are intrinsically more variable.

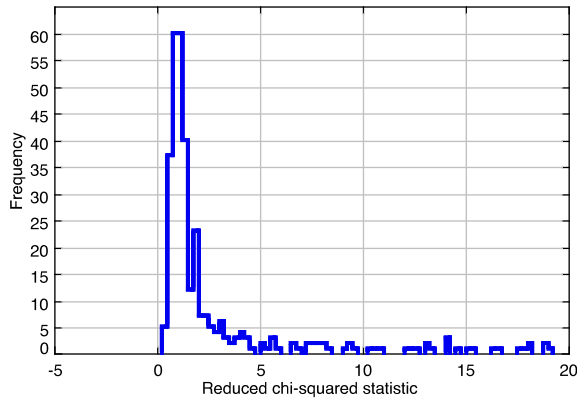


Fig. 6.— Variability distribution of the catalogue sources, shown in the form of the reduced χ^2 when the light curve is compared to a model of a constant mean flux.

3.4. Flux errors

As discussed in the previous section, the image reconstruction algorithm does not make a full correction for the off-axis response of the WFC cameras, resulting in a systematic increase in the flux uncertainty of $\sim 10\%$ in any given OP.

The mosaicing process generally reduces the effects of this poorly corrected off-axis response by averaging the fluxes from many OPs taken with different pointings, meaning that the source flux is measured at many different off-axis angles. However, in some cases where, for example, the single observations are not pointed with a random configuration (as in the galactic centre region) or when the source is highly variable, the fluxes in the maps could be affected by a systematic error higher than the estimated 10%. However, a plot of the source fluxes versus exposures, as in Figure 8, does not indicate any source flux

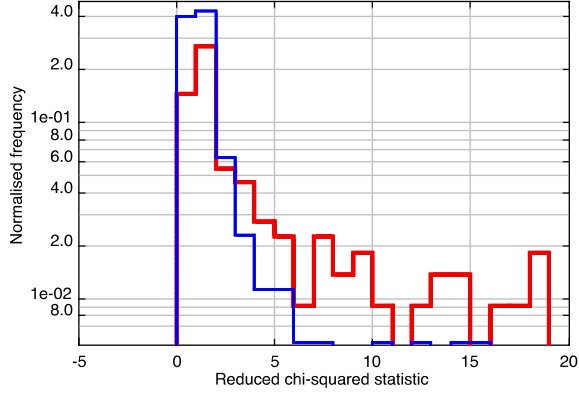


Fig. 7.— Blue histogram: distribution of the reduced χ^2 of the sources detected only in our catalogue. Red histogram: distribution of the reduced χ^2 of the sources detected in both our and the previous catalogue

anomalies. Thus the flux errors reported in Table 3 can be considered to include both the statistical and the systematic errors.

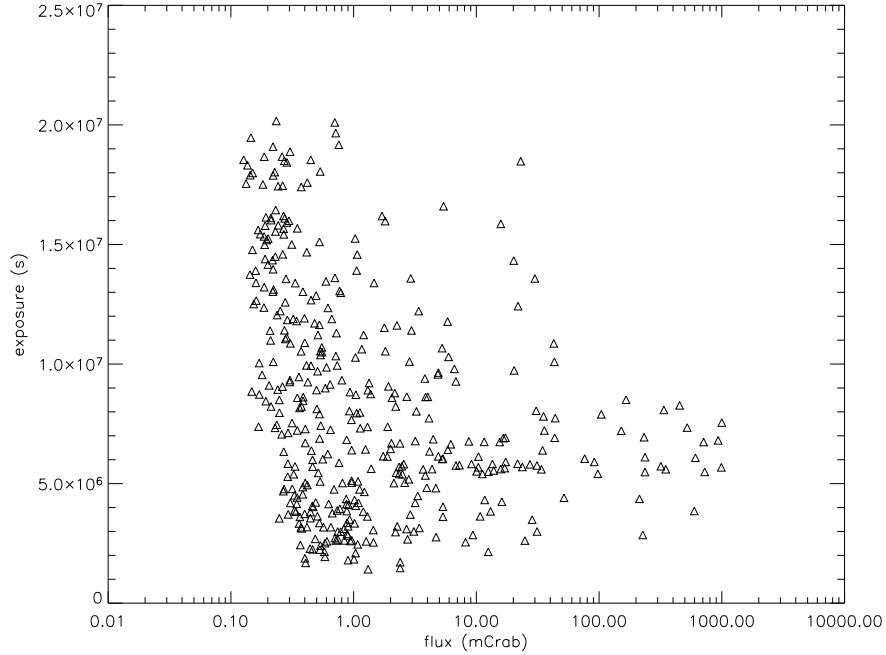


Fig. 8.— Exposure versus flux for each detected source. The sensitivity limit of the survey is clearly visible as the left border of the detected sources.

4. The source sample

In terms of the sources themselves, the WFC source type distribution from this work is significantly different from the one reported by the previous WFC catalogue and reflects the higher fraction of persistent sources in our catalog. This indicates that one must always be aware of the timescale of the sensitivity of surveys when using them - the hard X-ray sky varies on many timescales - and performing a source search on any one timescale inevitably introduces a bias towards different source types. In fact, as Figure 9 shows, our catalogue has a higher number of typical persistent objects like Seyfert 1 (Sy1), Seyfert 2 (Sy2) and Clusters of galaxies. In particular, compared to the previous catalogue, the number of Seyfert galaxies is increased by about 3 times for Sy1 and about 7 times for Sy2. While the number of Clusters of Galaxies detected increases by about 3 times.

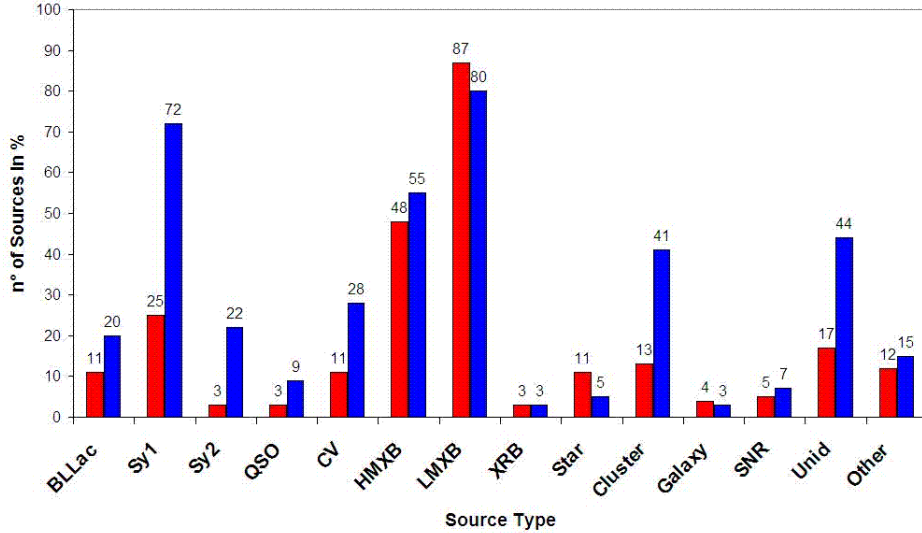


Fig. 9.— Source type distribution for this work (blue columns) compared with the one reported in Verrecchia et al. (2007) (red columns).

It is also noticeable that our catalog contains a higher number of unidentified sources with a distribution that traces the higher exposure zones of the map.

The low mass X-ray binaries are the most populated class of sources of this catalogue. Reflecting the highly variable nature of these objects, their number is slightly lower than the one previously reported (the total mosaic map lost the faintest transient objects) and all of them have been also detected in Verrecchia et al. (2007) except for 1E 1743.1-2843 that is a faint ($0.1-0.2 L_E$) and peculiar source classified as a LMXB with a persistent nature (Del Santo et al. 2006). 1E1743.1-2843 is a typical source for which our work is optimised.

The High Mass X-ray Binaries are mostly the same as those observed in the previous catalogue. The new detections (7 sources) are all Be/X-ray binary systems in which we caught either persistent or long-term outburst emission.

We detected 17 new Cataclismic Variables; looking at the different types of CV, mostly all the new objects found are IP (14 object for a total of 17), the CV subtype with the harder spectra (see e.g. Scaringi et al. (2010a)), while there are 3 new detections of Dwarf Novae out of a total of 5 sources (for a discussion on the hard X-ray spectra of DNs see Landi et al. in preparation).

Figure 10 shows the averaged hardness ratio (HR) of all the sources, extracted from both 3-17 keV and 17-28 keV mosaic maps. Even if the large errors only allow the extraction of basic information for faint sources, we can speculate about the global behaviour of the luminous sources.

The bright source sample is mostly formed by XRB; as Figure 10 shows, the HMXB are the hardest emitters: nine of them show a HR value greater than 3. The two softest HMXB are indeed LMC X-1 and LMC X-3, both of them are persistent sources often detected with a bright disc black body component (Yao et al. 2005). The hardest source of the entire sample is the HMXB GX301-2, one of the most massive X-ray binary known (see e.g. Leahy & Mostka (2009)), while the hardest LMXB is 1E1740.7-2942 (a persistent source often in hard state, Bouchet et al. (2009)) and GX1+4 an accreting X-ray pulsar (Ferrigno et al. 2007). However, for the most part, the LMXB have HR values that lie between 0.5 and 1.5. In particular the most luminous LMXBs show HR values below 1. This is in agreement with the expected behaviour of a LMXB which generally is very bright during its soft state (McClintock & Remillard 2005). The huge differences between the XRB hardness ratios are not only due to the intrinsic properties of these sources but are also due to the specific observations. With the XRBs being extremely variable, the averaged HR values depend strongly on the source spectral states at the time of the WFC observations and may not represent a real time-average hardness value.

We produced the logN-logS for the most populous source types present in our catalogue: the LMXB and HMXB. The distribution is only indicative because even if the sky coverage is virtually complete, the exposure is not uniform.

Our logN-logS distribution is consistent with the one reported in Grimm et al (2002) both for HMXB and for LMXB. As Figure 11 shows, the latter present a cutoff and a flatter behaviour with respect to the former. The straight lines in Figure 11 represent the lower and the upper limits of the best fit slopes reported by Grimm et al (2002). Our plot, above about two mCrab, is in good agreement with Grimm et al (2002) even if, in spite of a total

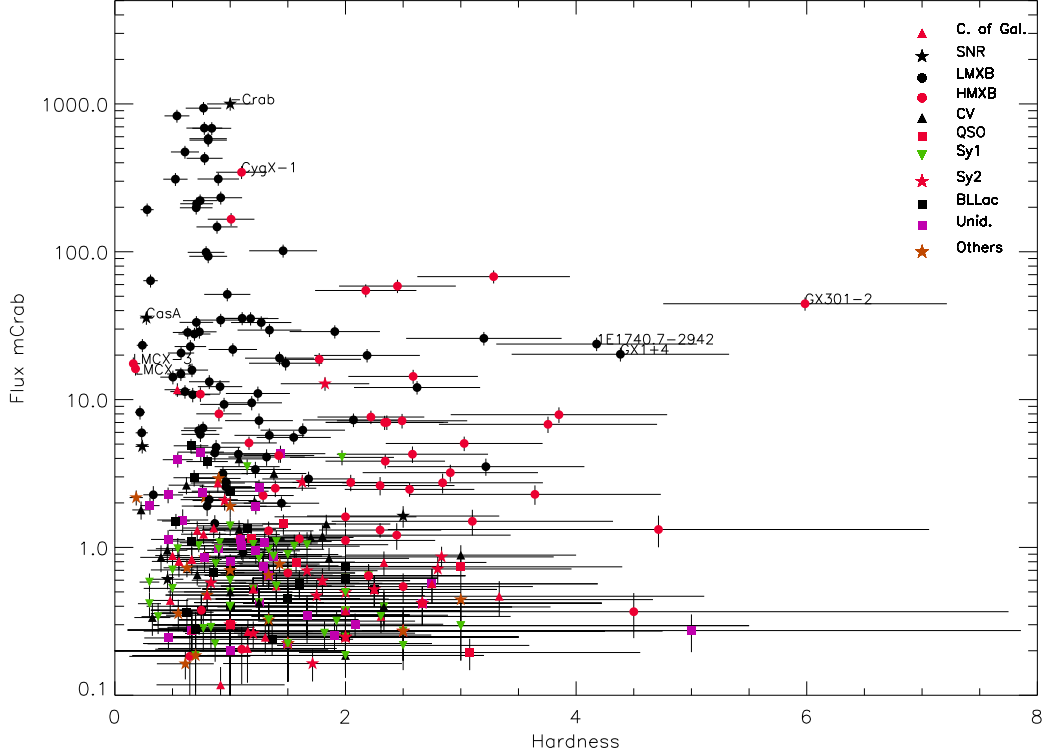


Fig. 10.— hardness ratio vs flux in mCrab. The hardness ratio is defined as $\text{Flux}_{17-28\text{keV}}/\text{Flux}_{3-17\text{keV}}$

sky coverage, no exposure correction has been added to our data: the exposure spans from 2×10^6 s to 20×10^6 s for LMXBs and 2.5×10^6 s to 15×10^6 s for HMXBs respectively.

4.1. Searching for transient sources with light curves

As discussed in section 3.3, we are able to extract (with some limitations) light curves for any point on the sky by extracting fluxes from the OP images. This method can be used to perform an additional search for and analysis of known sources, since it only needs the position of the selected source. As an example Figure 12 shows both WFC and ASM/RXTE light curves of the LMXB system XTE J1118+480.

This light curve tool is also useful to search for transient sources that are below the detection threshold in the total mosaic but are also too faint to be clearly detected in single OP images, falling somewhere between the capabilities of the two catalogues search methods.

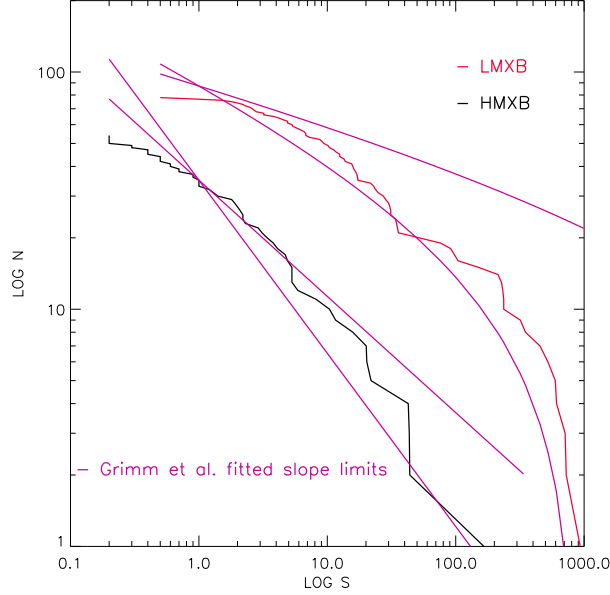


Fig. 11.— $\log N$ - $\log S$ distribution of respectively HMXB (black line) and LMXB (red line). The straight lines represent the lower and the upper limits of the best fit slopes reported by Grimm et al (2002). The fluxes are expressed in mCrab.

A good example of this is the case of IGR J17091-3624 (in 't Zand et al. 2002). This transient X-ray binary is not detected in the total mosaic but mosaicing only the WFCs observations near the known outburst periods (September 1996 and September 2001) the source is clearly detected (Capitanio, PhD Thesis 2007). Obviously this procedure implies that the position of the source and its outburst date(s) must be previously known, and this unfortunately significantly limits the application of this method.

4.2. The new source candidates

The new source candidates detected in the maps were chosen using three principal conservative criteria: a signal to noise ratio greater than 12 (set to cope with even the worst local sigma level in the mosaic map), an exposure higher than 4×10^6 s, the average exposure over the entire map, (see Section 2) and a light curve that does not present any spikes in single images. In fact we visually inspected several possible new transients and rejected all of them on the basis of their being at the image border or near a structure or presenting an unacceptable PSF. With our work being specifically optimised for faint persistent sources, we did not expect any new transient sources with respect to the previous catalogue that was

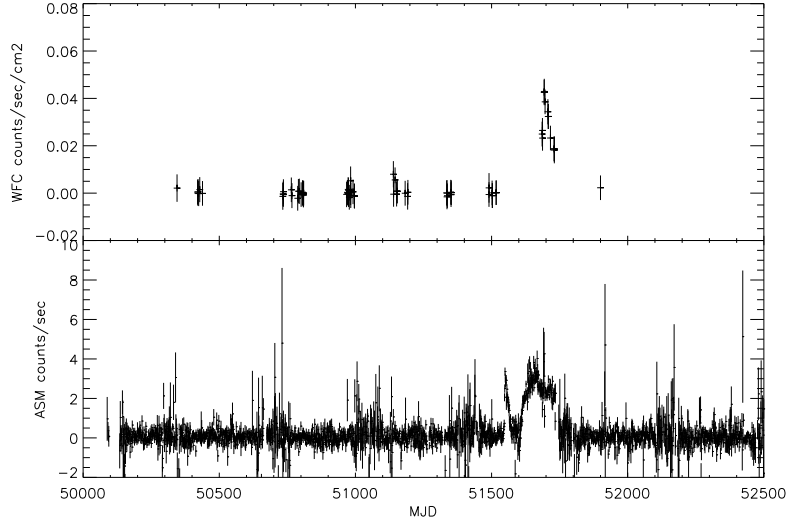


Fig. 12.— XTE J1118-480: top panel: WFC 3-17 keV light curve. Bottom panel: RXTE/ASM monitor light curve (1.3-12 keV)

optimised for transient detection. Applying these criteria, 10 new source candidates have been selected (3% of the total number of sources).

We searched for these 10 new sources within the X-ray observation archives and through catalogues from other energy ranges. The fields containing the new WFC sources have never been observed in the X-ray energy range below 20 keV (except for the ROSAT all sky survey that did not detect them) and they have not been detected above 20 keV in either Swift/BAT or IBIS/ISGRI mosaics.

Confidence in these 10 new detections is strongly supported by the many other sources uncovered by the same technique that proved to be correlated with known sources. Of course in this kind of work, it is always possible that some false detections will be included, and the new sources can only be truly verified by follow-up observations or detections in other instruments.

Table 4 summarises the principal characteristics of these 10 sources; in particular the last column reports the possible radio and infra-red counterparts of some of the sources.

Another source, WFC J1818-1658, was initially added to the list of the new sources, but after a more accurate analysis it was identified as the Supergiant fast X-ray transient SAX J1818-1703, as described below.

4.2.1. *The curious case of WFC J1818-1658/SAX J1818.6-1703*

SAX J1818.6-1703 is an anomaly within the WFC catalogs. This source, discovered by the WFC in 1998 (in 't Zand et al. 1998), was not automatically recognised in our mosaic map, and it is not reported in Verrecchia et al. (2007).

The best position found in the WFC map for our candidate WFC J1818-1658 lies $9.8'$ away from SAX J1818.6-1703 with a calculated error radius of $2'$, the source being detected at the 32.5 sigma level (in a sky zone with a local averaged background of about 10 sigma level). The source was automatically classified as a new source. A counterpart search in all *Swift*/XRT and XMM-Newton/EPIC data with the source in the field of view, did not discover any plausible counterpart within the $2'$ radius error circle. Although the position of WFC J1818-1658 is consistent with a serendipitous *XMM* source, 2XMMi J181813.9-165724, detected by both *Swift*/XRT and XMM-Newton/EPIC, the flux expected for a 32.5 sigma level source in the WFC mosaic map should be 100 times greater than that of this faint XMM object.

On the other hand, we know from IBIS studies (Bird et al. 2009) that SAX J1818.6-1703 (with counterparts clearly detected in most of the XRT and XMM images analysed) appears in the IBIS persistent search mosaics as a result of occasional outbursts and low-level emission that occur during its periastron passages every 30d.

Looking at each single WFC observation after the first detection of the source (in 't Zand et al. 1998), there is a faint transient object that appears recurrently in the data. This object has a position that slightly oscillates between the positions of the two sources (SAX J1818.6-1703 and WFC J1818-1658). However the periods in which the source is visible is recurrent and consistent with the known flaring period of SAX J1818-1703 (30 ± 1 days) (Bird et al. 2009; Zurita-Heras & Chaty 2009). Figure 13 shows some WFC single OP detections during both the flaring and the quiescent periods.

We can say that the timing analysis indicates that WFC J1818-1658 and SAX J1818-1703 have an high probability to be the same source and the shifted position of the SAX J1818.6-1703 is caused by the particular sky zone in which the source is situated. In fact this turns out to be a pathological case in which all the defects of the WFC map reported in the previous sections (i.e. Section 2.1) are manifest together: SAX J1818.6-1703 lies in the field of view of the periodic observations of the Galactic Centre region, thus the same star tracker configurations had been used each time. Moreover SAX J1818.6-1703 always lies at the border of these observations, thus at a huge off-axis angle. We have used mean offsets throughout this work when discussing position errors, because we are aware that there can be a small subset of sources (like SAX J1818-1703) that have substantially larger errors.

Quoting a 90% confidence limit based on this subset would give a misleadingly high location error for the vast majority of our sources. Finally, except for the first detection (~ 100 mCrab) (in 't Zand et al. 1998), the source flares were very faint (~ 1 mCrab), partly explaining why it has not been seen as a transient object, but is instead seen as a quasi-persistent emitter, just as it is in the IBIS survey analysis.

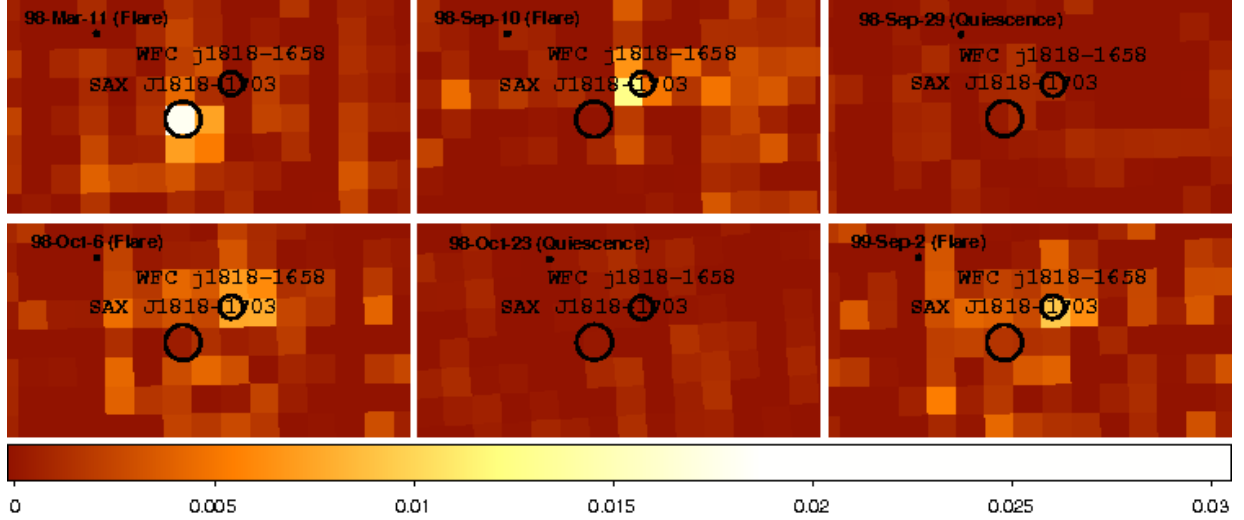


Fig. 13.— Selected WFC single-OP flux images, expressed in counts/s/cm^2 , of the SAX J1818-1703/WFC J1818-1658 region during both periodic flaring activity and quiescent states.

5. Concluding remarks

The wide field cameras on the BeppoSAX satellite were designed primarily to detect bright transient sources flaring within their large field of view. Despite this, the quality and quantity of data recorded has provided a legacy archive of quasi all-sky observations of the hard X-ray sky that has not been fully exploited.

We have successfully applied techniques developed for the *INTEGRAL*/IBIS survey to the BeppoSAX WFC dataset, on the basis that the two instruments are intrinsically similar in imaging method and operation. Our main aim has been to improve the sensitivity to weaker, more persistent sources not detected within individual WFC observations. The production and searching of mosaic maps from the ensemble of individual pointing is a good method to achieve this goal for persistent or quasi-persistent sources.

The success of this approach is evident in the detection of 182 sources not previously

recorded in WFC catalogs. Most of these are known sources, partly because of the surge in hard X-ray detections in the *INTEGRAL*/*Swift* era, but around 35 of these sources would have been new discoveries for BeppoSAX if found at the end of the mission. Even though this work is partly limited by the optimisation of the WFC hardware and software for transient source searching, this represents a success for the approach. From a technical viewpoint, the areas that could still be improved include the flux reconstruction for individual pointings (and hence light curve production) and the PSF distortion that limits the source location accuracy and useful energy range.

When used in combination with more recent all-sky hard X-ray surveys, this catalog provides a view of this highly variable sky in another epoch with similar sensitivity (better than 1mCrab), and as such should be of value in any studies of variability in galactic and extra-galactic hard X-ray sources.

Table 3:: BeppoSAX WFCs list of sources

Name ^a	Ra (°)	dec (°)	σ	error (') ^b	flux _(3–17keV) ^c	flux _(17–28keV) ^c	source type ^d	sub type ^e
IGR J00040+7020	0.913	70.307	7.7	3.3	0.2± 0.1	0.5± 0.1	Sy2	-
Mrk 335	1.591	20.199	7.4	3.3	0.4± 0.1	0.6± 0.1	Sy1	-
1RXS J000635.7-690030	1.660	-68.979	6.6	3.5	0.2± 0.1	0.4± 0.1	unid	-
QSO B0014+810	4.298	81.583	5.9	3.8	0.13± 0.03	0.4± 0.1	QSO	-
4U 0022+63	6.333	64.148	189.6	1.6	5.9± 0.6	1.4± 0.2	SNR	-
V709 Cas	7.177	59.278	31.6	2.0	1.0± 0.1	1.7± 0.2	CV	IP
IGR J00335+6126	8.346	61.428	5.6	3.9	0.2± 0.1	0.2± 0.1	unid	-
1RXS J003422.2-790525	8.540	-79.077	9.3	3.0	0.2± 0.1	0.5± 0.1	Sy1	-
1E S0033+59.5	8.920	59.804	39.3	1.9	1.3± 0.2	1.5± 0.2	BLLac	-
IGR J00370+6122	9.256	61.338	11.8	2.7	0.4± 0.1	0.3± 0.1	HMXB	-
RX J004241.6+411440	10.676	41.242	5.5	3.9	0.3± 0.1	0.2± 0.1	unid	-
NGC 262	12.147	31.951	5.8	3.8	0.3± 0.1	0.8± 0.2	Sy2	-
RX J0051.3-7216	12.802	-72.247	6.4	3.6	0.2± 0.1	0.13± 0.04	HMXB	-
RX J0052-7319	13.084	-73.321	8.7	3.1	0.3± 0.1	0.6± 0.1	HMXB	-
CF Tuc	13.290	-74.647	6.5	3.6	0.2± 0.1	-	RSCVn	-
XSS J00564+4548	13.838	46.202	6.2	3.7	0.3± 0.1	0.5± 0.1	CV	IP
gamma Cas.	14.165	60.702	156.0	1.6	4.9± 0.5	5.7± 0.6	HMXB	Be
XTE J0103-728	15.718	-72.740	7.2	3.4	0.2± 0.1	0.3± 0.1	HMXB	Be
PSR J0111-7317	17.850	-73.288	57.2	1.8	1.8± 0.2	4.6± 0.5	HMXB	Be
RX J0117.0-7326	19.292	-73.432	496.7	1.6	15.8± 1.6	28.0± 2.9	HMXB	SG
3A 0114+650	19.510	65.288	92.8	1.7	2.9± 0.3	6.8± 0.8	HMXB	SG
4U 0115+634	19.667	63.736	33.0	2.0	1.0± 0.1	2.3± 0.3	HMXB	Be
SWIFT J0123.9-5846	20.934	-58.820	11.9	2.7	0.5± 0.1	0.5± 0.1	Sy1	-
NGC 526	20.976	-35.067	16.4	2.4	0.8± 0.1	1.0± 0.2	Sy1	-
4U 0142+614	26.548	61.747	83.7	1.7	2.7± 0.3	0.5± 0.1	XRB	-
RX J0146.9+6121	26.789	61.342	62.0	1.8	2.1± 0.2	2.7± 0.3	HMXB	Be
1RXS J015634.6-835836	29.167	-83.987	12.4	2.6	0.3± 0.1	0.5± 0.1	unid	-
ICA 12	31.769	-74.429	7.9	3.2	0.2± 0.1	0.4± 0.1	StC.	-
IGR J02097+5222	32.418	52.450	10.4	2.8	0.4± 0.1	0.6± 0.1	Sy1	-
1H 0215-007	33.634	-0.772	7.7	3.3	0.4± 0.1	0.6± 0.1	Sy1	-
1ES 0212+735	34.357	73.801	5.8	3.8	0.22± 0.04	0.3± 0.1	BLLac	-
Mrk 1040	37.059	31.308	6.3	3.6	0.4± 0.1	0.8± 0.2	Sy1	-
SWIFT J0238.2-5213	39.595	-52.177	8.3	3.1	0.3± 0.1	0.2± 0.1	Sy1	-
1RXS J023832.6-311658	39.632	-31.267	9.1	3.0	0.4± 0.1	0.22± 0.04	QSO?	-
1E 0236.6+6100	40.178	61.237	4.8	4.3	0.2± 0.1	0.4± 0.1	HMXB	Be
QSO B0241+62	41.242	62.461	27.5	2.0	0.9± 0.1	1.2± 0.2	Sy1	-
4U 0253+4	43.602	41.575	12.1	2.6	0.7± 0.1	0.6± 0.1	Cluster	-
AC O401	44.739	13.587	8.1	3.2	0.5± 0.1	0.9± 0.2	Cluster	-
1E 0304.8+4045	47.052	40.950	39.6	1.9	2.2± 0.3	0.5± 0.1	RSCVn	-
QSO J0311-7651	47.955	-76.856	6.7	3.5	0.2± 0.1	0.6± 0.2	Sy1	-
RX J0317.9-4414	49.469	-44.233	13.8	2.5	0.5± 0.1	0.24± 0.03	Cluster	-

Continued on Next Page...

Table 3 – Continued

Name ^a	Ra (°)	dec (°)	σ	error (') ^b	flux _(3–17keV) ^c	flux _(17–28keV) ^c	source type ^d	sub type ^e
NGC 1275	49.949	41.516	231.9	1.6	13.1± 1.4	7.1± 0.7	Cluster	-
H 0324+28	51.627	28.693	16.1	2.4	1.1± 0.2	0.5± 0.1	RSCVn	-
PLX 728	52.809	43.886	23.0	2.1	1.2± 0.2	2.2± 0.3	CV	IP
HD 22468	54.202	0.583	16.5	2.4	1.0± 0.2	0.4± 0.1	RSCVn	-
EQ 0340-54	55.702	-53.614	10.7	2.8	0.4± 0.1	-	Cluster	-
IGR J03532-6829	58.233	-68.511	19.6	2.2	0.7± 0.1	0.6± 0.1	BLLac	-
X Per	58.859	31.072	121.3	1.7	8.2± 0.9	7.4± 0.8	HMXB	Be
Abell 478	63.360	10.467	14.5	2.5	0.9± 0.2	0.5± 0.1	Cluster	-
NGC 1566	64.972	-54.927	9.4	2.9	0.3± 0.1	0.5± 0.1	Sy1	-
SWIFT J0426.2-5711	66.532	-57.209	11.3	2.7	0.3± 0.1	0.23± 0.04	Sy1	-
Abell 3266	67.830	-61.426	14.9	2.4	0.4± 0.1	0.5± 0.1	Cluster	-
3C 120	68.280	5.373	13.7	2.5	0.9± 0.2	1.5± 0.3	Sy1	-
X 04333-1315	68.391	-13.273	8.7	3.1	0.5± 0.1	0.7± 0.2	Cluster	-
4U 0446+44	72.476	45.062	8.6	3.1	0.3± 0.1	0.5± 0.1	Cluster	-
RX J0452.0+4932	73.015	49.578	20.7	2.2	0.9± 0.1	1.2± 0.3	Sy1	-
1RXS J045602.3-753211	73.960	-75.529	10.4	2.8	0.3± 0.1	0.3± 0.1	Sy2	-
KMHK 414	74.563	-75.266	9.9	2.9	0.3± 0.1	-	StC	-
SWIFT J0505.8-2351	76.434	-23.821	7.6	3.3	0.4± 0.1	0.8± 0.2	Sy2	-
QSO B0502+675	76.998	67.621	20.2	2.2	0.7± 0.1	0.7± 0.1	BLLac	-
4U 0512-401	78.535	-40.059	113.3	1.7	3.2± 0.4	3.0± 0.3	LMXB	G
QSO B0513-002	79.032	-0.169	9.8	2.9	0.6± 0.1	0.9± 0.2	Sy1	-
ESO 362-018	79.881	-32.624	6.3	3.6	0.2± 0.1	0.2± 0.1	Sy1	-
PICTOR A	79.982	-45.785	8.0	3.2	0.2± 0.1	0.2± 0.1	Sy1	-
LMC X-2	80.052	-71.950	784.8	1.6	23.0± 2.3	13.2± 1.3	LMXB	Z
PKS J0522-3627	80.708	-36.447	6.7	3.5	0.2± 0.1	0.4± 0.1	BLLac	-
PKS J0525-6938	81.246	-69.651	9.1	3.0	0.3± 0.1	0.21± 0.04	SNR	-
AB Dor	82.169	-65.452	19.1	2.2	0.5± 0.1	0.4± 0.1	Star	K1IV
3A 0527-329	82.342	-32.810	31.1	2.0	1.1± 0.2	1.2± 0.2	CV	IP
RX J0531.2-6607	82.777	-66.102	8.5	3.1	0.2± 0.1	0.9± 0.2	HMXB	Be
LMC X-4	83.170	-66.376	121.3	1.7	3.4± 0.4	10.3± 1.1	HMXB	SG
Crab	83.616	21.999	19790.1	1.6	1000.0± 100.1	1000.0± 100.2	SNR	-
IGR J05346-5759	83.725	-58.029	19.4	2.2	0.5± 0.1	0.5± 0.17	CV	IP
AXS J053514-0523	83.828	-5.423	13.8	2.5	0.8± 0.1	0.8± 0.1	unid	-
LMC X-3	84.732	-64.085	819.8	1.6	21.9± 2.2	3.5± 0.4	HMXB	-
LMC X-1	84.957	-69.736	694.1	1.6	20.1± 2.0	3.6± 0.4	HMXB	SG
PSR B0540-69.3	85.030	-69.351	36.9	1.9	1.1± 0.1	1.2± 0.2	XRB	-
BY Cam	85.689	60.848	15.8	2.4	0.6± 0.1	0.8± 0.1	CV	P
TX Col	85.820	-40.987	5.1	4.1	0.15± 0.04	0.3± 0.1	CV	IP
QSO B0549-322	87.706	-32.267	11.3	2.7	0.4± 0.1	0.3± 0.1	BLLac	-
NGC 2110	88.047	-7.456	11.3	2.7	0.6± 0.1	1.0± 0.2	Sy2	-
1RXS J055229.5+592842	88.118	59.481	6.2	3.7	0.3± 0.1	0.3± 0.1	Sy1	-
4U 0558+46	88.747	46.428	28.5	2.0	1.1± 0.2	0.6± 0.1	Sy1	-

Continued on Next Page...

Table 3 – Continued

Name ^a	Ra (°)	dec (°)	σ	error (') ^b	flux _(3–17keV) ^c	flux _(17–28keV) ^c	source type ^d	sub type ^e
RX J0558.0+5353	89.456	53.872	7.7	3.3	0.3± 0.1	0.4± 0.1	CV	IP
4U 0557-385	89.494	-38.317	16.1	2.4	0.5± 0.1	0.8± 0.1	Sy1	(1.5)
QSO B0558-504	89.915	-50.431	12.7	2.6	0.3± 0.1	0.25± 0.03	Sy1	-
1RXS J061133.8-814917	92.956	-81.821	13.2	2.6	0.3± 0.1	0.6± 0.1	unid	-
4C 70.05	93.896	71.038	5.9	3.8	0.2± 0.1	0.5± 0.1	Sy2	-
4U 0614+091	94.282	9.125	556.4	1.6	35.8± 3.7	25.3± 2.6	LMXB	B
LEDA 75721	95.841	-64.595	6.1	3.7	0.26± 0.04	0.6± 0.2	Cluster	-
IGR J06253+7334	96.243	73.587	10.4	2.8	0.3± 0.1	0.6± 0.1	CV	IP
1ES 0625-53.6	96.567	-53.693	5.6	3.9	0.12± 0.04	0.11± 0.03	Cluster	-
QSO J0635-7516	98.944	-75.241	5.8	3.8	0.15± 0.04	0.3± 0.1	Sy1	-
1RXS J063847.2-535818	99.714	-53.962	6.1	3.7	0.26± 0.04	0.3± 0.1	Cluster	-
1ES 0644-54.1	101.405	-54.209	7.6	3.3	0.2± 0.1	0.2± 0.1	Cluster	-
1ES 0646-51.5	101.769	-51.590	8.2	3.2	0.2± 0.1	0.2± 0.1	unid	-
Mrk 6	103.051	74.426	13.2	2.5	0.3± 0.1	0.6± 0.1	Sy1	-
1ES 0657-55.8	104.606	-55.936	7.4	3.3	0.2± 0.1	0.23± 0.04	Cluster	-
1RXS J070912.3-152708	107.294	-15.454	8.0	3.2	0.3± 0.1	0.2± 0.1	unid	-
1RXS J071413.7-36	108.568	-36.423	5.5	3.9	0.2± 0.1	0.3± 0.1	unid	-
3A 0726-260	112.210	-26.100	17.2	2.3	0.6± 0.1	0.8± 0.1	HMXB	Be
SWIFT J0732.5-1331	113.154	-13.504	5.8	3.8	0.3± 0.1	0.5± 0.2	CV	IP
QSO B0738+499	115.613	49.846	10.4	2.8	0.5± 0.1	0.7± 0.1	Sy1	-
Sigma Gem.	115.803	28.885	9.3	3.0	0.7± 0.2	0.9± 0.2	RSCVn	-
1RXS J074616.8-161127	116.566	-16.171	6.4	3.6	0.3± 0.1	0.8± 0.2	unid	-
4U 0739-19	116.875	-19.301	23.3	2.1	1.0± 0.1	0.5± 0.1	Cluster	-
EXO 0748-676	117.088	-67.764	190.9	1.6	5.4± 0.6	8.8± 1.0	LMXB	B
IGR J07597-3842	119.933	-38.709	11.8	2.7	0.4± 0.1	0.5± 0.1	Sy1	-
ES O209-12	120.489	-49.768	9.2	3.0	0.3± 0.1	0.3± 0.1	Sy1	(1.5)
PG 0804+761	122.691	76.038	11.1	2.7	0.3± 0.1	0.4± 0.1	Sy1	-
RX J0812.4-3114	123.140	-31.245	26.5	2.1	1.0± 0.1	1.6± 0.2	HMXB	Be
XSS J08142+6231	123.150	62.620	9.2	3.0	0.4± 0.1	0.13± 0.03	CV	DN
CIZA J0812.5-5714	123.153	-57.244	9.9	2.9	0.3± 0.1	0.3± 0.1	Cluster	-
ACO 644	124.363	-7.513	8.6	3.1	0.6± 0.1	1.4± 0.3	Cluster	-
1ES 0821-42.6	125.823	-42.850	15.3	2.4	0.5± 0.1	0.6± 0.1	unid	-
RX J0825.2+7306	126.300	73.106	14.4	2.5	0.4± 0.1	0.5± 0.1	CV	DN
1RXS J082627.1-640421	126.493	-64.069	7.1	3.4	0.2± 0.1	0.2± 0.1	unid.	-
1ES 0826-70.3	126.628	-70.553	8.5	3.1	0.2± 0.1	0.3± 0.1	unid	-
RX J0832.4+3707	128.143	37.131	5.0	4.2	0.2± 0.1	0.2± 0.1	Sy1	-
Vela Pulsar	128.815	-45.183	59.5	1.8	1.9± 0.2	2.3± 0.3	SNR	-
LEDA 24297	129.635	-35.990	6.2	3.7	0.2± 0.1	0.4± 0.1	Sy1	-
QSO B0836+710	130.347	70.894	33.4	1.9	1.1± 0.1	1.3± 0.2	QSO	-
Vela X-1	135.519	-40.530	1173.9	1.6	43.9± 4.4	144.2± 14.6	HMXB	SG
IGR J09026-4812	135.683	-48.211	6.3	3.6	0.2± 0.1	0.6± 0.2	Sy1	-
X 0906-0931	137.250	-9.689	8.4	3.1	0.6± 0.1	0.8± 0.2	Cluster	-

Continued on Next Page...

Table 3 – Continued

Name ^a	Ra (°)	dec (°)	σ	error (′) ^b	flux _(3–17keV) ^c	flux _(17–28keV) ^c	source type ^d	sub type ^e
SWIFT J0917.2-6221	139.020	-62.313	13.2	2.6	0.4± 0.1	0.6± 0.1	Sy1	-
4U 0918-549	140.114	-55.210	228.4	1.6	6.6± 0.7	4.8± 0.5	LMXB	B
3A 0921-630	140.640	-63.299	49.4	1.8	1.5± 0.2	1.3± 0.2	LMXB	D
RX J0923.7+2254	140.915	22.896	5.9	3.8	0.4± 0.1	0.6± 0.2	Sy1	-
X 0922-314	141.084	-31.700	89.3	1.7	4.4± 0.5	2.4± 0.3	unid	-
SDSS J092514.05+522112.7	141.309	52.354	9.5	2.9	0.4± 0.1	0.4± 0.19	QSO	-
LEDA 97526	141.511	-84.348	6.8	3.5	0.14± 0.04	0.24± 0.04	Sy2	-
NGC 2992	146.396	-14.329	7.0	3.4	0.5± 0.1	0.9± 0.2	Sy2	-
4U 0945-30	146.902	-30.933	42.1	1.9	2.1± 0.3	2.0± 0.3	Sy2	-
NGC 3031	148.968	69.063	18.0	2.3	0.6± 0.1	0.3± 0.1	Sy1	-
M 82	148.969	69.671	23.0	2.1	0.8± 0.1	0.5± 0.1	Galaxy	-
GRO J1008-57	152.451	-58.307	16.8	2.3	0.5± 0.1	1.1± 0.2	HMXB	Be
IGR J10101-5654	152.548	-56.928	7.3	3.4	0.2± 0.1	0.22± 0.04	HMXB	Be
1RXS J101015.9-311909	152.571	-31.364	8.3	3.1	0.4± 0.1	0.9± 0.2	BLLac	-
SWIFT J1010.1-5747	152.788	-57.821	9.9	2.9	0.3± 0.1	0.7± 0.1	CV	Symb
NGC 3227	155.875	19.862	8.1	3.2	0.6± 0.1	1.2± 0.3	Sy1	-
QSO B1029-140	157.964	-14.282	5.9	3.8	0.3± 0.1	0.5± 0.1	QSO	-
4U 1036-56	159.397	-56.791	16.4	2.4	0.5± 0.1	1.0± 0.2	HMXB	Be
SWIFT J1038.8-4942	159.698	-49.777	5.8	3.8	0.2± 0.1	0.14± 0.04	Sy1	-
IGR J10404-4625	160.064	-46.431	6.8	3.5	0.2± 0.1	-	Sy2	-
IGR J10448-5945	161.251	-59.700	91.2	1.7	3.0± 0.3	2.7± 0.3	Star	EtaCar
1RXS J110337.7-232931	165.894	-23.495	10.2	2.8	0.4± 0.1	0.4± 0.1	BLLac	-
Mrk 421	166.126	38.203	142.1	1.6	5.3± 0.6	3.5± 0.4	BLLac	-
NGC 3516	166.706	72.582	34.5	1.9	1.0± 0.1	1.2± 0.2	Sy1	-
XTE J1118+480	169.580	48.064	60.3	1.8	2.6± 0.3	2.5± 0.3	LMXB	M
Cen X-3	170.318	-60.615	1207.2	1.6	42.7± 4.3	92.9± 9.4	HMXB	Be
1H 1121-591	171.140	-59.259	19.6	2.2	0.7± 0.1	0.32± 0.05	SNR	-
IGR J11366-6002	174.202	-60.090	5.7	3.9	0.2± 0.1	0.5± 0.2	AGN?	-
NGC 3783	174.765	-37.754	31.4	2.0	1.4± 0.2	1.4± 0.2	Sy1	-
HD 101379	174.834	-65.403	65.0	1.8	2.3± 0.3	1.8± 0.2	Star	-
V* V1033 Cen	175.327	-64.183	13.5	2.5	0.5± 0.1	0.6± 0.1	CV	P
SWIFT J1142.7+7149	175.901	71.702	16.6	2.3	0.5± 0.1	0.6± 0.1	CV	IP
IGR J11435-6109	176.009	-61.123	14.9	2.4	0.6± 0.1	0.9± 0.2	HMXB	Be
RX J1145.2+7940	176.294	79.687	13.2	2.5	0.3± 0.1	0.6± 0.1	Sy1	-
H 1143-182	176.432	-18.460	10.5	2.8	0.5± 0.1	1.0± 0.2	Sy1	-
1E 1145.1-6141	176.847	-61.961	148.9	1.6	5.3± 0.6	12.4± 1.3	HMXB	SG
2E 1145.5-6155	176.993	-62.196	32.1	2.0	1.2± 0.2	1.6± 0.2	HMXB	Be
RX J1155.4-5641	178.851	-56.722	7.6	3.3	0.3± 0.1	0.5± 0.1	CV	DN
NGC 3998	179.496	55.451	7.4	3.3	0.3± 0.1	0.4± 0.1	AGN	liner
IGR J12026-5349	180.723	-53.839	5.8	3.8	0.2± 0.1	0.4± 0.1	Sy2	-
NGC 4151	182.649	39.407	88.1	1.7	3.3± 0.4	6.5± 0.7	Sy1	-
1RXS J121222.7-580118	183.130	-58.010	7.7	3.3	0.3± 0.1	0.5± 0.1	unid	-

Continued on Next Page...

Table 3 – Continued

Name ^a	Ra (°)	dec (°)	σ	error (') ^b	flux _(3–17keV) ^c	flux _(17–28keV) ^c	source type ^d	sub type ^e
EXMS B1210-645	183.308	-64.887	50.0	1.8	1.8± 0.2	2.2± 0.3	unid	-
SAX J1221.7+7526	185.529	75.385	8.8	3.0	0.2± 0.1	0.4± 0.1	Sy2	-
GX 301-2	186.707	-62.776	562.6	1.6	20.3± 2.1	121.5± 12.4	HMXB	SG
3C 273	187.272	2.041	19.7	2.2	2.4± 0.4	2.4± 0.4	BLLac	-
IGR J12349-6434	188.771	-64.557	15.4	2.4	0.6± 0.1	1.8± 0.3	CV	Symb
IGR J12415-5750	190.348	-57.826	9.1	3.0	0.4± 0.1	0.7± 0.2	Sy2	(1.5)
1H 1249-637	190.673	-63.049	19.6	2.2	0.7± 0.1	0.9± 0.1	HMXB	Be
Abell 3526	192.207	-41.316	17.3	2.3	0.9± 0.1	0.5± 0.1	Cluster	-
4U 1246-58	192.389	-59.072	167.9	1.6	6.8± 0.7	5.2± 0.6	LMXB	B
RX J1252.4-2914	193.122	-29.256	52.6	1.8	2.9± 0.4	1.8± 0.2	CV	IP
4U 1254-690	194.395	-69.308	881.1	1.6	30.0± 3.0	20.7± 2.1	LMXB	B
ACO 1656	194.928	27.965	23.7	2.1	1.3± 0.2	1.0± 0.1	Cluster	-
IGR J13020-6359	195.473	-63.974	12.2	2.6	0.4± 0.1	1.0± 0.2	HMXB	Be?
1RXS J131651.8-715537	199.261	-71.913	12.2	2.6	0.4± 0.1	0.5± 0.1	unid	-
NGC 5128	201.359	-43.008	199.2	1.6	10.7± 1.1	19.5± 2.1	Sy2	-
4U 1323-62	201.605	-62.127	110.7	1.7	4.9± 0.5	7.6± 0.8	LMXB	B
RXC J1327.9-3130	202.040	-31.468	7.6	3.3	0.4± 0.1	0.9± 0.2	Cluster	-
MCG-06-30-015	203.983	-34.289	17.6	2.3	1.0± 0.2	1.4± 0.2	Sy1	-
1ES 1344-326	206.888	-32.838	24.1	2.1	1.4± 0.2	1.0± 0.2	Cluster	-
Abell 1795	207.226	26.612	17.9	2.3	0.9± 0.1	0.7± 0.1	RGal	-
3A 1346-301	207.334	-30.306	56.0	1.8	3.4± 0.4	3.9± 0.5	Sy1	-
Mrk 279	208.264	69.321	20.2	2.2	0.8± 0.1	0.4± 0.1	Sy1	-
GS 1354-645	209.495	-64.733	41.2	1.9	1.8± 0.2	2.6± 0.3	LMXB	BHC
1RXS J140041.2-632623	210.220	-63.445	13.2	2.6	0.6± 0.1	0.8± 0.2	unid	-
Circinus Gal.	213.293	-65.342	12.1	2.6	0.5± 0.1	1.4± 0.3	Sy2	-
NGC 5506	213.302	-3.233	37.7	1.9	2.4± 0.3	3.9± 0.5	Sy2	-
1RXS J141656.0-120053	214.200	-11.981	5.9	3.8	0.4± 0.1	1.1± 0.3	unid	-
2E 1415+2556	214.495	25.704	8.0	3.2	0.4± 0.1	0.6± 0.1	BLLac	-
NGC 5548	214.515	25.125	16.8	2.3	0.8± 0.1	0.7± 0.1	Sy1	(1.5)
H 1417-624	215.302	-62.706	44.5	1.9	2.2± 0.3	6.4± 0.8	HMXB	Be
NSC J142605+374853	216.535	37.806	7.6	3.3	0.3± 0.1	1.0± 0.2	Cluster	-
H 1426+428	217.151	42.659	11.3	2.7	0.5± 0.1	1.0± 0.2	BLLac	-
SAX J1428.6-5422	217.214	-54.390	37.7	1.9	2.4± 0.3	3.0± 0.4	unid	-
WFC J1452-5708	223.913	-57.146	13.7	2.5	1.0± 0.2	1.3± 0.2	unid	-
IGR J15094-6649	227.455	-66.831	14.2	2.5	0.7± 0.1	0.9± 0.2	CV	IP
Abell 202	227.755	5.741	13.0	2.6	0.9± 0.2	0.6± 0.1	Cluster	-
PSR B1509-58	228.494	-59.156	26.8	2.0	1.9± 0.3	1.9± 0.3	XP	-
ACO 2052	229.198	6.984	5.7	3.9	0.4± 0.1	1.1± 0.3	Cluster	-
QSO B1517+656	229.381	65.417	10.5	2.8	0.4± 0.1	0.25± 0.03	BLLac	-
Cir X-1	230.152	-57.171	10565.0	1.6	933.1± 93.5	502.3± 50.4	LMXB	A
RXC J1539.5-8335	234.934	-83.585	19.7	2.2	0.4± 0.1	-	unid	-
4U 1538-522	235.601	-52.367	123.6	1.7	10.4± 1.1	26.9± 3.0	HMXB	SG

Continued on Next Page...

Table 3 – Continued

Name ^a	Ra (°)	dec (°)	σ	error (') ^b	flux _(3–17keV) ^c	flux _(17–28keV) ^c	source type ^d	sub type ^e
XTE J1543-568	235.982	-56.776	23.5	2.1	1.9± 0.3	5.4± 0.8	HMXB	Be
4U 1543-624	236.967	-62.544	489.5	1.6	30.7± 3.1	22.5± 2.3	LMXB	-
XTE J1550-564	237.706	-56.484	929.2	1.6	76.3± 7.7	23.6± 2.4	LMXB	M
PG 1553+113	238.939	11.168	6.7	3.5	0.5± 0.1	1.5± 0.4	QSO	-
PKS J1557-7913	239.212	-79.228	9.4	2.9	0.2± 0.1	0.3± 0.1	Sy2	-
Abell 2142	239.617	27.247	22.7	2.1	1.1± 0.2	1.2± 0.2	Cluster	-
1H 1556-605	240.273	-60.730	255.2	1.6	17.2± 1.8	11.5± 1.2	LMXB	-
XSS J16019-7548	240.369	-75.756	19.8	2.2	0.5± 0.1	0.4± 0.1	Cluster	-
4U 1608-522	243.152	-52.415	159.2	1.6	13.8± 1.5	11.3± 1.2	LMXB	A
MCG+14-08-004	244.876	81.035	5.8	3.8	0.18± 0.04	0.11± 0.02	Galaxy	-
SCO X-1 ²	244.975	-15.624	-	-	LMXB	Z		
RX J1625.5+8529	246.740	85.492	6.4	3.6	0.16± 0.03	0.4± 0.1	Sy1	-
4U 1624-490	247.001	-49.171	547.9	1.6	51.8± 5.3	50.5± 5.2	LMXB	D
Abell 2199	247.190	39.550	27.9	2.0	0.9± 0.1	0.6± 0.1	Cluster	-
AX J1631.9-4752	248.004	-47.883	10.1	2.9	1.0± 0.2	3.1± 0.6	HMXB	-
ACO 3628	247.808	-75.135	9.4	2.9	0.3± 0.1	0.3± 0.1	Cluster	-
4U 1626-67	248.066	-67.456	128.5	1.7	5.8± 0.6	12.0± 1.3	LMXB	-
4U 1630-47	248.529	-47.394	115.5	1.7	11.7± 1.3	7.9± 0.9	LMXB	BHC
ACO 2218	248.954	66.207	6.3	3.6	0.2± 0.1	0.4± 0.1	Cluster	-
IGR J16377-6423	249.582	-64.358	26.4	2.1	1.4± 0.2	1.2± 0.2	Cluster	-
WFC J1640-2001	250.068	-20.018	32.9	2.0	4.7± 0.6	3.5± 0.5	unid	-
ACO 2219	250.076	46.713	10.0	2.9	0.3± 0.1	-	Cluster	-
4U 1636-536	250.207	-53.752	2550.6	1.6	213.4± 21.4	150.5± 15.1	LMXB	-
GX 340+0	251.435	-45.623	4296.7	1.6	452.9± 45.4	352.4± 35.4	LMXB	-
WFC J1649-1818	252.307	-18.302	28.7	2.0	3.9± 0.5	5.6± 0.8	unid	-
Mrk 501	253.466	39.778	128.8	1.7	4.0± 0.4	3.2± 0.4	BLLac	-
GRO J1655-40	253.479	-39.836	2286.6	1.6	232.7± 23.4	65.1± 6.6	LMXB	-
IGR J16558-5203	254.032	-52.062	13.6	2.5	1.1± 0.2	1.0± 0.2	Sy1	-
Her X-1	254.467	35.337	245.5	1.6	8.7± 0.9	22.8± 2.4	LMXB	-
OA0 1657-415	255.186	-41.673	42.0	1.9	4.1± 0.5	15.4± 2.0	HMXB	SG
H 1658-298	255.494	-29.955	135.6	1.7	12.5± 1.3	11.4± 1.22	LMXB	-
GX 339-4	255.665	-48.786	182.8	1.6	16.1± 1.7	8.1± 0.9	LMXB	-
ACO 2244	255.690	34.073	8.0	3.2	0.3± 0.1	0.2± 0.1	Cluster	-
EXSS 1706.6+7842	255.992	78.620	29.7	2.0	0.7± 0.1	1.0± 0.1	Cluster?	-
4U 1700-377	255.998	-37.859	439.9	1.6	43.5± 4.5	106.6± 11.0	HMXB	SG
GX 349+2	256.429	-36.416	6965.4	1.6	711.3± 71.3	597.8± 60.0	LMXB	-
4U 1702-429	256.542	-43.054	378.3	1.6	35.2± 3.6	32.3± 3.3	LMXB	-
4U 1700+24	256.640	23.959	16.0	2.4	0.9± 0.1	1.0± 0.2	LMXB	-

Continued on Next Page...

²data containig SCOX-1 were too noisy to be added in the total mosaic map

Table 3 – Continued

Name ^a	Ra (°)	dec (°)	σ	error (') ^b	flux _(3–17keV) ^c	flux _(17–28keV) ^c	source type ^d	sub type ^e
4U 1705-440	257.219	-44.130	1154.2	1.6	104.3± 10.5	82.5± 8.3	LMXB	-
RX J1709.5-2639	257.347	-26.686	24.6	2.1	2.2± 0.3	1.8± 0.3	LMXB	-
EXMS B1707-375	257.753	-37.618	9.5	2.9	0.9± 0.2	0.7± 0.1	unid	-
SAX J1711.6-3808	257.928	-38.109	35.4	1.9	3.2± 0.4	3.9± 0.5	LMXB	-
WFC J1712-2639	258.057	-26.660	26.6	2.0	2.3± 0.3	0.7± 0.1	unid	-
4U 1708-40	258.073	-40.851	183.0	1.6	16.6± 1.7	9.5± 1.0	LMXB	-
OPH CLUSTER	258.095	-23.378	28.4	2.0	2.8± 0.4	2.5± 0.3	Cluster	-
SAX J1712.6-3739	258.136	-37.664	48.2	1.8	4.5± 0.5	3.9± 0.5	LMXB	-
NSC J171252+640307	258.189	64.052	9.8	2.9	0.3± 0.1	0.21± 0.04	Cluster	-
2S 1711-339	258.578	-34.029	55.7	1.8	4.9± 0.6	4.3± 0.5	LMXB	-
XTE J1716-389	258.983	-38.859	132.2	1.7	11.6± 1.3	8.6± 1.0	HMXB	SG
RX J1719.2+4858	259.838	48.989	7.5	3.3	0.26± 0.04	0.5± 0.1	Sy1	-
FIRST J172201.9+431523	260.465	43.256	6.1	3.7	0.23± 0.04	-0.2± -0.1	Sy1	-
XTE J1723-376	260.896	-37.687	73.0	1.7	6.2± 0.7	4.6± 0.5	LMXB	-
RX J1723.8+8553	261.309	85.881	8.9	3.0	0.23± 0.04	0.3± 0.1	Cluster	-
4U 1724-307	261.866	-30.791	357.6	1.6	27.3± 2.8	36.6± 3.8	LMXB	G
QSO B1727+502	262.063	50.235	11.2	2.7	0.3± 0.1	0.21± 0.04	BLLac	-
HD 159023	262.165	59.056	14.0	2.5	0.3± 0.1	-	Star	-
GX 9+9	262.934	-16.951	2277.3	1.6	236.4± 23.8	174.8± 17.6	LMXB	-
GX 354-0	262.984	-33.860	1189.2	1.6	91.5± 9.2	133.5± 13.5	LMXB	-
GX 1+4	263.020	-24.719	135.8	1.7	11.2± 1.2	49.1± 5.3	LMXB	-
1ES 1734+74.2	263.241	74.238	10.4	2.8	0.3± 0.1	0.3± 0.1	RSCVn	-
4U 1730-335	263.351	-33.389	286.7	1.6	21.7± 2.2	22.2± 2.3	LMXB	G
KS 1731-260	263.573	-26.088	1251.6	1.6	97.6± 9.9	79.0± 8.0	LMXB	-
SLX 1735-269	264.574	-26.990	94.1	1.7	6.8± 0.8	8.5± 1.0	LMXB	-
WFC J1738-3336	264.613	-33.601	35.1	1.9	2.6± 0.3	1.2± 0.2	unid	-
4U 1735-444	264.724	-44.467	1926.8	1.6	151.4± 15.2	134.1± 13.5	LMXB	-
1RXS J174018.3-205103	265.111	-20.840	27.9	2.0	2.5± 0.3	1.9± 0.3	unid	-
XTE J1739-278	265.687	-27.749	103.7	1.7	7.3± 0.8	1.7± 0.2	LMXB	-
2MASX J17431735+6250207	265.811	62.822	6.7	3.5	0.25± 0.04	0.3± 0.1	Sy2	-
1E 1740.7-2942	265.956	-29.728	200.5	1.6	13.5± 1.4	56.4± 5.9	LMXB	-
1RXS J1744.1+3259	266.061	32.987	8.5	3.1	0.3± 0.1	0.5± 0.1	unid	-
GRO J1744-28	266.156	-28.756	256.6	1.6	17.0± 1.8	54.4± 5.7	LMXB	-
1A 1742-294	266.534	-29.520	355.0	1.6	23.7± 2.4	45.2± 4.7	LMXB	-
1E 1743.1-2843	266.573	-28.733	35.1	1.9	2.3± 0.3	7.4± 1.0	LMXB	-
SAX J1747.0-2853	266.719	-28.869	138.0	1.7	9.1± 1.0	10.8± 1.2	LMXB	-
SLX 1744-299	266.879	-30.029	254.2	1.6	17.3± 1.8	24.7± 2.6	LMXB	-
GX 3+1	266.969	-26.572	4335.2	1.6	318.5± 31.9	285.6± 28.7	LMXB	-
EXO 1745-248	267.028	-24.781	442.4	1.6	33.9± 3.5	39.9± 4.1	LMXB	G
4U 1745-203	267.225	-20.357	43.2	1.9	3.8± 0.5	5.0± 0.6	LMXB	G
4U 1746-370	267.528	-37.075	458.4	1.6	34.6± 3.5	38.2± 3.9	LMXB	G
SAX J1750.8-2900	267.565	-29.035	36.8	1.9	2.5± 0.3	4.2± 0.5	LMXB	-

Continued on Next Page...

Table 3 – Continued

Name ^a	Ra (°)	dec (°)	σ	error (') ^b	flux _(3–17keV) ^c	flux _(17–28keV) ^c	source type ^d	sub type ^e
GRS 1747-312	267.684	-31.285	76.1	1.7	5.3± 0.6	7.1± 0.8	LMXB	G
GX 5-1	270.307	-25.086	11222.9	1.6	991.4± 99.3	761.9± 76.4	LMXB	-
GRS 1758-258	270.308	-25.731	192.6	1.6	15.8± 1.7	23.4± 2.5	LMXB	-
GX 9+1	270.383	-20.520	7216.2	1.6	725.5± 72.8	562.7± 56.4	LMXB	-
SAX J1808.4-3658	272.149	-36.980	24.8	2.1	2.0± 0.3	1.6± 0.2	LMXB	-
GX 13+1	273.625	-17.141	3095.4	1.6	349.4± 35.1	183.5± 18.4	LMXB	-
4U 1812-12	273.779	-12.101	90.6	1.7	10.4± 1.2	12.9± 1.4	LMXB	-
GX 17+2	274.019	-14.015	5025.8	1.6	609.8± 61.1	493.3± 49.5	LMXB	-
AM Her	274.061	49.869	114.2	1.7	2.9± 0.3	4.0± 0.4	CV	P
SAX J1818-1703/WFC J1818-1658 ³	-16.970	32.5	2.0	3.7± 0.5	3.0± 0.4	unid	-	-
1RXS J182129.0-131641	275.331	-13.308	15.5	2.4	1.7± 0.3	1.0± 0.2	unid	-
QSO J1821+6420	275.504	64.342	24.5	2.1	0.6± 0.1	0.6± 0.1	Sy1	-
4U 1820-303	275.927	-30.374	2772.3	1.6	236.6± 23.8	217.3± 21.9	LMXB	G
4U 1822-000	276.333	-0.029	309.2	1.6	24.9± 2.6	16.3± 1.7	LMXB	-
4U 1822-371	276.477	-37.113	182.9	1.6	15.5± 1.6	33.9± 3.6	LMXB	-
GS 1826-24	277.362	-23.784	312.9	1.6	31.2± 3.2	39.6± 4.1	LMXB	-
SNR 021.5-00.9	278.382	-10.559	12.4	2.6	1.2± 0.2	3.0± 0.5	SNR	-
3C 382	278.761	32.680	27.9	2.0	1.1± 0.1	0.8± 0.1	Sy1	-
RX JB1832-330	278.926	-33.020	49.0	1.8	4.2± 0.5	4.5± 0.5	LMXB	G
1H 1828-593	279.222	-59.400	12.2	2.6	0.6± 0.1	0.5± 0.1	Sy2	-
ESO 103-35	279.553	-65.434	13.9	2.5	0.6± 0.1	1.7± 0.3	Sy2	-
Ser X-1	279.978	5.052	2934.4	1.6	227.1± 22.8	161.0± 16.2	LMXB	-
3C 390.3	280.628	79.777	33.3	1.9	0.8± 0.1	1.0± 0.1	Sy1	-
RX J184452-62215	281.201	-62.383	11.9	2.7	0.5± 0.1	1.1± 0.2	Sy1	-
Ginga 1843+009	281.413	0.823	60.7	1.8	4.7± 0.6	18.1± 2.1	HMXB	Be
4U 1916-79	281.750	-78.532	11.6	2.7	0.3± 0.1	0.7± 0.1	Sy1	-
IGR J18483-0311	282.073	-3.211	11.1	2.7	0.9± 0.2	2.2± 0.4	HMXB	-
3A 1845-024	282.088	-2.461	17.1	2.3	1.4± 0.2	5.1± 0.8	HMXB	Be
IGR J18485-0047	282.144	-0.731	9.0	3.0	0.7± 0.2	0.9± 0.2	unid	-
4U 1850-087	283.270	-8.694	28.8	2.0	2.8± 0.4	2.7± 0.4	LMXB	G
1E 1846.5-7857	283.722	-78.907	7.4	3.3	0.26± 0.04	0.6± 0.1	Sy1	-
XTE J1855-026	283.909	-2.622	7.9	3.2	0.7± 0.2	3.3± 0.7	HMXB	-
XTE J1856+053	284.169	5.321	34.7	1.9	2.7± 0.4	0.9± 0.1	LMXB	-
1E 1849.2-7832	284.362	-78.463	8.2	3.1	0.22± 0.04	0.4± 0.1	Sy1	-
XTE J1859+226	284.673	22.653	210.8	1.6	10.1± 1.1	2.2± 0.2	LMXB	-
XTE J1901+014	285.412	1.449	9.0	3.0	0.7± 0.2	0.7± 0.1	XRB	-
WFC J1907+1305	286.943	13.088	12.7	2.6	0.9± 0.2	1.1± 0.1	unid	-
1ES 1907+52.3	287.084	52.425	7.9	3.2	0.2± 0.1	0.14± 0.02	RSCV	-

Continued on Next Page...

³see Section 4.2.1

Table 3 – Continued

Name ^a	Ra (°)	dec (°)	σ	error (') ^b	flux _(3–17keV) ^c	flux _(17–28keV) ^c	source type ^d	sub type ^e
4U 1907+097	287.413	9.830	68.3	1.7	5.3± 0.6	13.2± 1.5	HMXB	SG
WFC J1909+1246	287.497	12.769	14.7	2.4	1.0± 0.2	0.9± 0.2	unid	-
4U 1909+07	287.723	7.608	38.7	1.9	3.1± 0.4	8.0± 1.0	HMXB	-
AX J1911.0+0906	287.785	9.088	16.4	2.4	1.3± 0.2	0.6± 0.1	unid	-
Aql X-1	287.831	0.597	366.1	1.6	31.2± 3.2	19.7± 2.0	LMXB	-
SS 433	287.961	4.988	27.1	2.0	2.3± 0.3	3.2± 0.4	HMXB	SG
IGR J19140+0951	288.510	9.864	12.1	2.6	0.9± 0.2	1.8± 0.3	HMXB	SG
GRS 1915+105	288.818	10.948	7057.8	1.6	596.3± 59.7	482.5± 48.4	LMXB	-
4U 1916-053	289.684	-5.234	107.6	1.7	9.4± 1.0	8.9± 1.0	LMXB	-
4U 1919+44	290.292	43.960	33.7	1.9	1.2± 0.2	1.3± 0.2	Cluster	-
ESO 141-55	290.339	-58.680	16.5	2.4	0.8± 0.1	1.1± 0.2	Sy1	-
V* CH Cyg	291.129	50.237	7.3	3.4	0.2± 0.1	0.3± 0.1	CV	Symb
RX J1927.3+6533	291.857	65.556	10.2	2.8	0.3± 0.1	0.4± 0.1	Sy1	-
WFC J1929+1720	292.250	17.338	17.3	2.3	1.0± 0.2	1.1± 0.2	unid	-
WFC J1933+1408	293.252	14.141	17.2	2.3	1.1± 0.2	1.2± 0.2	unid	-
WFC J1935+2053	293.996	20.894	15.7	2.4	0.8± 0.1	1.1± 0.2	unid	-
XTE J1946+274	296.403	27.329	115.2	1.7	5.3± 0.6	12.5± 1.4	HMXB	Be
1RXS J194708.6-762335	296.734	-76.403	8.4	3.1	0.2± 0.1	0.3± 0.1	unid	-
KS 1947+300	297.390	30.172	45.7	1.8	2.0± 0.3	4.6± 0.6	HMXB	Be
XSS J19303-7950	297.486	-79.764	8.2	3.2	0.21± 0.04	0.4± 0.1	unid.	-
4U 1954+319	298.947	32.096	128.2	1.7	5.9± 0.6	13.1± 1.4	HMXB	-
Cyg X-1	299.578	35.220	6690.7	1.6	337.1± 33.78	370.4± 37.2	HMXB	M
4U 1957+115	299.850	11.702	379.8	1.6	28.5± 2.9	6.8± 0.7	LMXB	-
Cyg A	299.859	40.713	30.6	2.0	1.3± 0.2	1.9± 0.3	QSO	-
QSO B1959+650	300.046	65.159	62.7	1.8	1.7± 0.2	0.9± 0.1	BLLac	-
SWIFT J2009.0-6103	302.189	-61.110	9.1	3.0	0.4± 0.1	0.4± 0.1	Sy1	-
QSO J2009-4849	302.374	-48.827	77.2	1.7	3.2± 0.4	2.2± 0.3	BLLac	-
1E S2008-57.0	303.078	-56.849	12.6	2.6	0.5± 0.1	0.6± 0.1	Cluster	-
RX J2012.6+3809	303.216	38.161	11.4	2.7	0.5± 0.1	0.6± 0.1	LMXB	-
RX J2014.4+6123	303.620	61.401	6.9	3.5	0.2± 0.1	0.2± 0.1	unid.	-
EXO 2030+375	308.061	37.627	25.7	2.1	1.3± 0.2	2.6± 0.4	HMXB	Be
Cyg X-3	308.136	40.948	3438.0	1.6	165.7± 16.6	167.0± 16.8	HMXB	-
LEDA 64989	308.649	-30.632	6.8	3.5	0.4± 0.1	0.4± 0.1	Sy1	-
4C 74.26	310.674	75.121	28.3	2.0	0.7± 0.1	1.1± 0.2	QSO	-
Mrk 509	311.060	-10.733	16.2	2.4	1.0± 0.2	0.9± 0.1	Sy1	-
1RXS J204937.4-800800	312.323	-80.128	10.0	2.9	0.2± 0.1	0.3± 0.1	RSCV	-
1RXS J205528.2-002123	313.877	-0.365	8.7	3.1	0.6± 0.1	1.2± 0.3	BLLac	-
IGR J202569+4940	314.167	49.680	18.9	2.2	0.6± 0.1	0.8± 0.1	AGN?	-
GRO J2058+42	314.734	41.782	11.0	2.7	0.5± 0.1	1.1± 0.2	HMXB	Be
SAX J2103.5+4545	315.920	45.736	56.5	1.8	2.2± 0.3	4.5± 0.5	HMXB	Be
1RXS J210604.3+614322	316.553	61.755	5.2	4.1	0.28± 0.04	0.13± 0.04	unid.	-
XSS J21128+8216	318.529	82.092	20.3	2.2	0.4± 0.1	0.8± 0.1	Sy1	-

Continued on Next Page...

Table 3 – Continued

Name ^a	Ra (°)	dec (°)	σ	error (') ^b	flux _(3–17keV) ^c	flux _(17–28keV) ^c	source type ^d	sub type ^e
IGR J21247+5058	321.153	50.981	23.1	2.1	0.8± 0.1	1.2± 0.2	Sy1	-
SWIFT J2127.4+5654	321.934	56.947	13.5	2.5	0.4± 0.1	0.5± 0.1	Sy1	-
4U 2129+12	322.512	12.176	180.9	1.6	12.5± 1.3	7.6± 0.8	LMXB	G
1RXS J213202.3-334255	323.023	-33.719	11.2	2.7	0.5± 0.1	0.7± 0.1	Sy1	-
IGR J21335+5105	323.426	51.122	12.4	2.6	0.4± 0.1	0.5± 0.1	CV	IP
QSO J2136-6224	324.129	-62.394	6.6	3.5	0.3± 0.1	0.6± 0.2	Sy1	-
1RXS J213833.0+320507	324.671	32.096	7.7	3.3	0.5± 0.1	0.15± 0.02	Sy1	-
SS Cyg	325.660	43.595	89.0	1.7	3.9± 0.4	4.2± 0.5	CV	DN
Cyg X-2	326.174	38.325	8269.0	1.6	522.2± 52.3	317.4± 31.8	LMXB	-
PKS J2151-3027	327.975	-30.477	6.6	3.6	0.3± 0.1	0.3± 0.1	QSO	Blazar
PKS J2157.6941	329.265	-69.692	6.6	3.5	0.2± 0.1	0.3± 0.1	Sy1	-
PKS J2158-3013	329.742	-30.242	23.5	2.1	1.2± 0.2	0.8± 0.1	BLLac	-
1RXS J220157.8-595648	330.463	-59.949	8.2	3.2	0.3± 0.1	0.6± 0.1	Cluster	-
NGC 7172	330.491	-31.865	6.0	3.8	0.3± 0.1	0.8± 0.2	Sy2	-
4U 2206+543	332.019	54.512	116.2	1.7	3.8± 0.4	5.4± 0.6	HMXB	Be
2E 2206.1-4724	332.338	-47.189	12.0	2.6	0.5± 0.1	0.6± 0.1	Sy1	-
RX J2214.0+1242	333.529	12.689	10.6	2.8	0.7± 0.1	1.3± 0.3	CV	DN
V* FO Aqr	334.474	-8.350	15.2	2.4	1.0± 0.2	1.8± 0.3	CV	IP
1RXS J223355.0-843406	338.685	-84.588	7.9	3.2	0.24± 0.04	0.5± 0.1	unid.	-
NGC 7314	338.937	-26.016	7.5	3.3	0.4± 0.1	0.15± 0.02	Sy1	-
4U 2238+60	339.812	61.261	9.0	3.0	0.3± 0.1	0.8± 0.2	HMXB	Be
Ark 564	340.661	29.752	14.7	2.4	0.7± 0.1	0.21± 0.03	Sy1	-
IM peg	343.302	16.829	14.1	2.5	0.7± 0.1	0.5± 0.1	RSCVn	-
3C 454.3	343.484	16.153	6.2	3.7	0.3± 0.1	0.9± 0.2	Star	-
QSO B2251-178	343.535	-17.573	11.5	2.7	0.8± 0.2	1.1± 0.2	Sy1	-
1AXG J225518-0310	343.846	-3.189	22.4	2.1	1.3± 0.2	1.4± 0.2	CV	IP
2E 2259.0+5836	345.299	58.881	12.4	2.6	0.4± 0.1	0.3± 0.1	HMXB	-
1RXS J230238.1+713649	345.654	71.613	8.2	3.2	0.2± 0.1	-	unid	-
NGC 7469	345.791	8.874	14.7	2.5	0.9± 0.2	1.4± 0.2	Sy1	-
NGC 7582	349.600	-42.351	9.7	2.9	0.4± 0.1	0.9± 0.2	Sy2	-
Cas A	350.885	58.831	1271.2	1.6	43.2± 4.4	11.8± 1.2	SNR	-
II Peg	358.788	28.639	7.3	3.4	0.3± 0.1	0.7± 0.2	RSCVn	-
PKS J2357-3445	359.235	-34.769	9.9	2.9	0.5± 0.1	0.6± 0.1	Cluster	-
H 2356-309	359.810	-30.616	10.4	2.8	0.5± 0.1	0.8± 0.2	BLLac	-
1RXS J000053.0-783038	359.987	-78.523	6.1	3.7	0.14± 0.04	0.7± 0.2	unid	-

Continued on Next Page...

Table 3 – Continued

Name ^a	Ra ($^{\circ}$)	dec ($^{\circ}$)	σ	error ($'$) ^b	flux _(3–17keV) ^c	flux _(17–28keV) ^c	source type ^d	sub type ^e
--------------------------	--------------------------	---------------------------	----------	-----------------------------------	---	--	---------------------------------	------------------------------

^aa name in bold face indicates a new detection with respect to Verrecchia et al. (2007).

^berror circle radius extrapolated from Figure 5 with the systematic error included.

^caverage flux estimation in mCrab (see Section 4.1 for details).

^dType classifications: AGN=Active galactic nuclei; BLLac=BL Lac object; Cluster=Cluster of galaxies; CV=Cataclysmic variable; HMXB=High-mass X-ray binary; LMXB=Low-mass X-ray binary; QSO = Quasar; RGal=Radio Galaxy; RSCVn= RS Canum Venaticorum variable; SNR=Supernova remnant; Sy1=Seyfert 1 galaxy; Sy2=Seyfert 2 galaxy; Unid=Unidentified source; StC=Star Cluster XRB=Galactic X-ray binary; XP=X-ray pulsar;

^eSub Type classifications: A=Atoll-type source (neutron Star); B=Burster (neutron star); Be=B-type emission-line star; BHC=Black hole candidate; D=Dipping; DN= Dwarf Nova; G=Globular Cluster X-ray source; IP=Intermediate Polar; M=microquasar P=Polar; Symb=Symbiotic star; SG=Supergiant; Z=Z-type source;

Table 4: *WFC new source candidates*

Name	R.A.	Dec	sigma	err. rad.	exposure	possible counterpart ¹
-	Deg.	Deg.	-	arcmin	s×10 ⁶	-
WFC J1452-5708	223.913	-57.146	13.7	2.5	7.5	2MASS J14553991-5710008
WFC J1640-2001	250.068	-20.018	32.9	2.0	4.6	-
WFC J1649-1818	252.307	-18.302	28.7	2.0	4.6	-
WFC J1712-2639	258.057	-26.660	26.6	2.0	5.2	-
WFC J1738-3336	264.613	-33.601	35.1	1.9	5.6	2MASS J17381495-3335373
WFC J1907+1305	286.943	13.088	12.7	2.6	4.0	-
WFC J1935+2053	293.996	20.894	15.7	2.4	4.9	2MASS J19360455+2055306
WFC J1909+1246	287.497	12.769	14.7	2.4	3.9	-
WFC J1929+1720	292.250	17.338	17.3	2.3	4.8	-
WFC J1933+1408	293.252	14.141	17.2	2.3	4.5	-

The authors would like to thank the Rome section of the IASF-INAF institute for the financial support. Special thanks also go to the ASI Data center staff and in particular to Francesco Verrecchia for the useful BeppoSAX WFC material made available on line through the ADSC web site. The authors acknowledge financial contribution from the agreement ASI-INAF I/009/10/0 and I/033/10/0. FC also thanks the Physics Department of *Università degli studi Roma 3* for the kind hospitality.

REFERENCES

- Bertin, E., & Arnouts, S. 1996, 117, 393.
- Bird, A. J. et al., 2010, ApJS, 186,1
- Bird, A. J. et al., 2009, MNRAS, 393, L11
- Bird, A. J. et al. 2007, ApJS, 170, 175.
- Bird, A. J. et al. 2006, ApJ, 636, 765
- Bird, A. J. et al. 2004, ApJ, 607, L33
- Boella, G., Butler R.C., Perola, C., Piro, L., Scarsi, L., Bleeker, J. A. M., 1997, A&AS, 122, 299.
- Bouchet, L., del Santo, M., Jourdain, E., Roques, J. P., Bazzano, A., DeCesare, G., 2009, ApJ, 693, 1871
- Capitanio, F., Bird, A. J., Bazzano, A., Ubertini, P., 2010, PoS, The Extreme Sky: Sampling the Universe above 10 keV, 013, available in <http://pos.sissa.it>

- Capitanio, F., Bird, A. J., Federici, M., Bazzano, A., Ubertini, P., 2008, AIPC,1010, 257
- Capitanio, F., Bazzano, A., Cocchi, M., 2004, Nuc. Phys. B. 132, 580
- Caroli, E., Stephen, B., Di Cocco, G. Space Science Reviews, 1987 45, 349.
- Courvoisier, T. J. L. et al. 2003, A&A, 411, L343.
- Del Santo, M., Sidoli, L., Bazzano, A., Cocchi, M., De Cesare, G., Paizis, A., Ubertini, P. 2006, A&A, 456, 1105.
- Ebisawa, K., Bourban, G., Bodaghee, A., Mowlavi, N., Courvoisier, T. J.-L. et al. 2003, A&A, 411, L59
- Ferrigno, C., Segreto, A., Santangelo, A., Wilms, J., 2007, A&A 462,995
- Grimm,H.-J.,Gilfanov1, M., and Sunyaev, R. 2002, A&A 391, 923
- in 't Zand, J. J. M. 1992, PhD Thesis, University Utrecht
- in 't Zand, J. J. M.,Heise, J., Jager, R., 1994, A&A, 288, 665
- in 't Zand, J. J. M., Heise, J., Smith, M., Muller, J. M., Ubertini, P., Bazzano, A., 1998, IAU Circ. 6840, p. 2
- in 't Zand, J. J. M.,Heise, J., Ubertini, P. Bazzano, A., Markwardt, C., 2004, ESA SP-552, 463, February 2004, Proceeding of the 5th *INTEGRAL* workshop
- Jager, R. et al., 1997, A&AS, 125, 557
- Jager, R., Schuurmans, J. J., n 't Zand, J. J. M., Heise, J. 1992 ASPC, 25, 154.
- Leahy, D. A, Kostka, M., 2009, MNRAS, 384, 747
- McClintock, J. E. & Remillard, R. A., 2005, *in Compact Stellar X-ray Sources*, Cambridge Univ Press.
- Piro, L. & Scarsi, L., 2004, Nuc Phys. B, 132, 1
- Revnivtsev, M., Sazonov, S., Jahoda, K. and Gilanov, M., 2004, A&A, 418, 927
- Scaringi, S., Bird, A. J., Norton, A. J., Knigge, K., Hill, A. B., Clark, D. J., Dean, A. J., McBride, V. A., Barlow, E. J., Bassani, L., Bazzano, A., Fiocchi, M. ans Landi, R., 2010, MNRAS, 401, 2218.

- Scaringi, S., Bird, A. J., Hill, A. B. Clark, D. J., McBride, V. A., Dean, A. J., Bazzano, A., Natalucci, L., Stephen, J. B., 2010, *A&A*, 516, 75
- Tramutola, A., Montagna, M., Martella, P., Bacchetta, A. 2000, *ESASP*, 425, 443
- Tueller, J., Baumgartner, W. H., Markward, C. B. et al. 2010, *ApJS*, 186, 378
- Ubertini, P. et al. 2003, *A&A*, 411, L131
- Verrecchia, F., in 't Zand, J. J. M., Giommi, P., Santolamazza, P., Granata, S., Schuurmans, J. J., Antonelli, L. A., 2007, *A&A* 472 705
- Vetere, L., Soffitta, P., Massaro, E., Giommi, P., Costa, E., 2007, *A&A*, 473, 347
- Voges, W., Aschenbach, B., Boller, Th. et al. 1999, *A&A*, 349, 389
- Yao, Y., Wang, Q. D., Zhang, N. S., 2005, *NMRAS*, 362, 229
- Winkler, C. et al. 2003, *A&A*, 411, L1
- Zurita-Heras, J. A., & Chaty, S. 2009, *A&A*, 493, L1